Evaporation Hysteresis over Vegetation

The Impact of Surface Processes and Boundary Layer Dynamics

G.E. de Groot

TU Delft

WAGENINGEN
UNIVERSITY & RESEARCH

Evaporation Hysteresis over Vegetation

The Impact of Surface Processes and Boundary Layer Dynamics

by

G.E. de Groot

to obtain the degree of Master of Science
at the Delft University of Technology,
to be defended publicly on 12 July 2019 at 10:00

Student number:	4759648	
Project duration:	December 15, 2018 – July 12, 2019	
Thesis committee:	Prof. dr. ir. B. J. H. van de Wiel	TU Delft, supervisor
	Dr. S. R. de Roode	TU Delft
	Dr. ir. A.M.J. Coenders	TU Delft
	Prof. dr. J. Vilà-Guerau de Arellano	Wageningen University

TU Delft

WAGENINGEN
UNIVERSITY & RESEARCH

Abstract

The non-linear relation between Evapotranspiration (ET) and the atmospheric moisture demand in terms of vapor pressure deficit (*VPD*) has been widely reported. Observations point towards a diverse range of potential drivers; however, without uncovering why the identified factors are found to control diurnal ET-*VPD* hysteresis. Modelling efforts have laid a theoretical foundation to unravel the compound effect of surface and atmospheric states on this hysteresis. However, so far these models have been unable to realistically incorporate the non-linear feedbacks between atmosphere and surface, and lack a vegetation representation that reflects the underlying biological mechanisms. To unravel in what manner the characteristics of ET-*VPD* hysteresis are controlled, multi-scale observations spanning biology, meteorology, and hydrology from the CloudRoots campaign are combined with modelling in a novel manner. For the first time a proof-of-concept is delivered for reproducing ET-*VPD* hysteresis with a model that incorporates both surface-atmosphere feedbacks as well as a mechanistic vegetation component. Observations are used for parameter initialization and evaluation to ensure that the modelled hysteresis curve and underlying processes represent a realistic case. Next, this calibrated model is used for a sensitivity analysis. The results show that both the early morning state of the surface and the state of the atmosphere influence the characteristics of the hysteresis loop with respect to its width, height, and initial slope. Via control of the stomatal aperture, soil moisture stress and the vegetation's capacity to assimilate CO_2 for photosynthesis affect the height and width of the curve. The height of the hysteresis loop is significantly affected by entrainment of warm dry air, while its width is minorly impacted. The characteristic fingerprint of entrainment is distinctly different to that of soil moisture stress and the capacity for CO_2 uptake. The sensitivity analysis applied to our observationally inspired case, appears to facilitate quantification of the strongest model responses to changing external forcings and parameters. Therefore, the presented approach offers a promising tool, allowing further research into the controlling mechanisms of ET-*VPD* hysteresis.

Contents

1 Introduction

The aim of this study is to investigate how surface and atmospheric processes control evapotranspiration (ET). ET drives the water cycle, sets the energy available for the diurnal temperature evolution, and regulates countless biochemical reactions. However, it still is a strikingly uncertain factor in atmospheric and hydrological modelling. Recent publications on the hysteretic relationship between ET and atmospheric moisture demand open the way for approaching the challenge of accurately representing ET in a novel way. In order to understand how the hysteretic relationship is set we cannot rely on observational analysis alone, as many processes and interactions are involved. Furthermore a solid theoretical foundation is lacking. Therefore this study will combine observations with prognostic modelling and integrate biology, hydrology, and meteorology, to link hysteresis characteristics to surface and atmospheric processes. Thereby delivering a new research method, progressing our mechanistic understanding, and ultimately allowing for a better representation of ET in models.

1.1. Relevance

ET affects our lives every day: It has a large influence on temperature, cloud formation, precipitation, and on the global climate (Chahine, 1992; Pielke, 2001; Wang, 2012). It determines the amount of water that is available for plants to flourish and to produce food. Or controls drought and flooding, which frequently result in humanitarian crisis and conflict. Furthermore, the magnitude of ET has an impact on the water content in the soil, vegetation, and atmosphere, where water is indispensable as a reagent and solvent in countless biochemical reactions. And ET affects the partitioning of net available energy at the surface between the sensible and latent heat fluxes, as well as the associated turbulent mixing and development of clouds. Therefore, understanding and accurately representing ET in atmospheric models is of major importance, both for day-to-day weather prediction as well as for long term climate and water availability forecasts (Held and Soden, 2000; Parlange et al., 1995; Schneider et al., 2010; Sellers et al., 1997; Sherwood et al., 2010). However, identifying the dominant driver of ET is difficult as many environmental variables - e.g. air temperature, net radiation, relative humidity, wind speed, soil moisture - and surface conditions - e.g. soil type, vegetation species, senescence - contribute to its diurnal evolution, and further research is required (Katul, 2012; Wang, 2012).

One of the effects that needs further study is the diurnal hysteresis between ET and the atmospheric moisture demand over vegetated surfaces (Zhang, 2014), as shown in Figure 1.1. Although over land surfaces this hysteresis is inherent to the evolution of the atmospheric layer where the impact of the surface is felt (the so-called boundary layer, BL), soil water depletion models generally assume a linear relationship as would be the case in open water conditions where one can assume vapor saturation at the surface (Marshall and Plumb, 1989). This assumption leads to errors in soil water availability estimates and associated decision making for irrigation and drainage. Including an estimate for the hysteresis magnitude in these models will therefore yield a significant improvement.

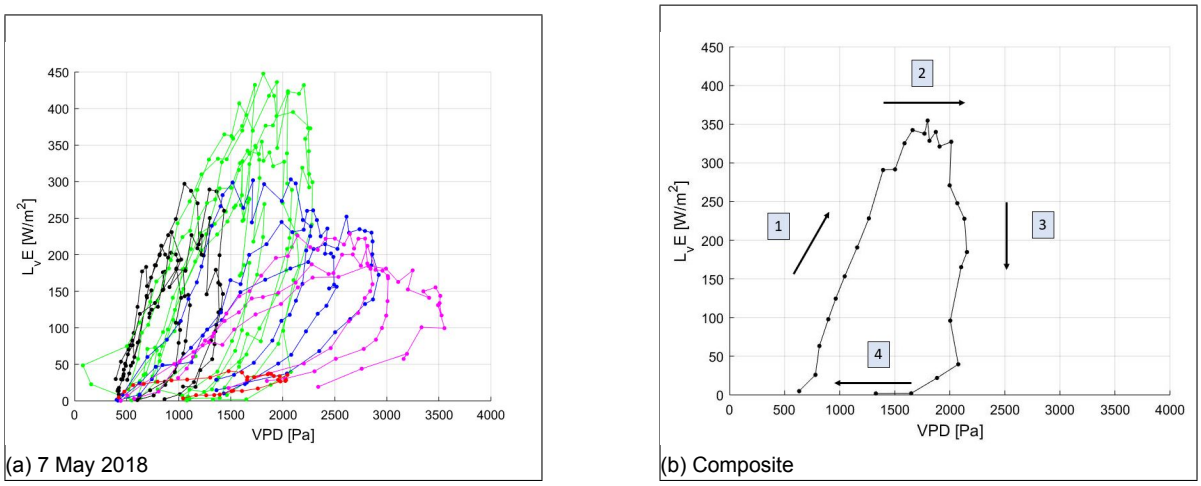

Figure 1.1: Diurnal hysteresis between ET and atmospheric moisture demand, measured with Eddy Covariance (EC) at the measurement site near Selhausen, Germany. ET is quantified as latent heat flux (L_vE [W m^{-2}]), and atmospheric demand as vapor pressure deficit (*VPD* [Pa]). (a) Composite of multiple diurnal loops where different colours indicate similar parameter regimes; Green: May 7-8-12-21-26 and June 6; Blue: June 10-28-29; Purple: July 1-2-3; Red: July 9; Black: May 11-18-19 and June 9 2018. (b) Single hysteresis loop for 7 May 2018 where four stages are identified. (1) Morning: The vegetation's stomata are maximally open for photosynthesis, the BL grows, ET is driven by the available radiation and *VPD* by temperature; (2) Early afternoon: Reduced stomatal aperture limits further ET increase, whereas *VPD* increase still is controlled by temperature, the BL stops growing; (3) Afternoon: Stomata close due to stress and ET drops to zero while VPD remains approximately constant due to competing temperature and moisture effects, the BL height remains approximately constant; and (4) Evening and night: Closed stomata prevent ET and *VPD* rapidly decreases due to decreasing temperatures, the BL shrinks. A full description is given in Chapters 1.2.1 and 3.1.

The second motivation for investigating the relationship between ET and the atmospheric moisture demand is that it reflects the state of both the surface and the atmosphere. Though hysteresis itself is inherent to BL evolution over land surfaces (Gutierrez, 1994), its fingerprint is a reflection of the very processes controlling this evolution; as much on the local - via e.g. surface temperature, humidity, and soil moisture stress - as on the non-local scale - via the growth of the atmospheric layer where the impact of the surface is felt (boundary layer, BL), entrainment, and subsidence. These processes are in turn the result of surface and atmospheric states. As such, the ET-moisture demand hysteresis shape can be a powerful method to disentangle the impact of the processes driving the diurnal course of ET.

Therefore this study investigates the relationship between ET and atmospheric moisture demand. ET depends on the soil, vegetation, and near-surface atmospheric processes, whereas moisture demand is an atmospheric variable. The work addresses the integration of surface and near-surface processes with atmospheric ones, while taking into account horizontal variability of the surface. The work will go beyond the existing theoretical foundation and will demonstrate how hysteresis shape is sensitive to key characteristics of the surface, the BL and external forcings.

1.2. Theoretical Background

To study the diurnal hysteresis between ET and the atmospheric moisture demand, ET is often quantified as latent heat flux (L_vE [W m^{-2}]), and atmospheric moisture demand as vapor pressure deficit (*VPD* [Pa]). Where *VPD* is set by the difference of the temperature driven saturation pressure and the moisture driven vapor pressure (Chapter 1.2.2).

ET-*VPD* hysteresis is typical for land surfaces and occurs when changes in turbulent mixing and ability of the surface to excrete water cause ET to differ significantly between morning and afternoon for the same magnitude of *VPD*, as shown in Figure 1.1b. For vegetated surfaces the clockwise tendency is a result of stomatal response to the environment. Conversely, under very dry desert conditions the direction of the loop is reversed to an anti-clockwise pattern, set only by turbulent mixing between surface and atmosphere (recent work by F. Lobos

Roco, paper in preparation). To analyse both the hysteresis directionality and shape, this chapter introduces the key concepts and equations needed to understand how turbulent mixing and the surface biology impact hysteresis appearance.

1.2.1. Conceptual Description of Stomatal Behaviour

For vegetated surfaces the non-linear relation between transpiration and *VPD* is mainly driven by changes in stomatal aperture: The aperture balances the benefits of maximizing CO_2 assimilation for photosynthesis with the detriments of transpiration (Cowan and Farquhar, 1977). The stomatal aperture, and consequently ET, responds to the availability of photosynthetically active radiation (*PAR* [W m^{-2}]), temperature, soil moisture availability, *VPD*, and the CO_2 deficit between the stomatal cavity and surrounding air. For the diurnal ET-*VPD* cycle, as shown in Figure 1.1b for the 7 May 2018 observations, four stages can be identified that can conceptually be understood by:

1. In the morning transpiration is controlled by the opening of the stomata in response to the increasing of *PAR*, allowing photosynthesis. Due to the increasing *PAR*, the canopy releases moisture into the atmosphere at an increasing rate. However, *VPD* increases rather than decreases: The overall rapid rise in BL temperature causes the higher saturation pressure to dominate the behaviour of *VPD* (Equation 1.1). In addition, the latent and sensible heat (H [W m^{-2}]) fluxes cause the BL to grow rapidly: Water vapor is distributed over a larger BL volume and warm, dry air is entrained at the BL top, effectively out-competing the effect of ET on specific humidity. (Moeng and Wyngaard, 1984)

2. Typically around midday transpiration has increased to a rate where it becomes difficult for plants to maintain their internal water paths, and the stomata reduce their aperture to prevent tissue damage (Hsiao, 1973). At this time, the sensible heat flux causes the air temperature to increase, and consequently also the saturation pressure and *VPD*.

3. As less *PAR* is available for photosynthesis, or leaf temperature or *VPD* becomes too high, the trade-off between the CO_2 demand for photosynthesis and cost of water loss becomes unfavourable. The stomata close in order to protect the plant water paths and avoid tissue damage. ET now rapidly drops to zero. The BL is no longer growing or heating, and the *VPD* remains approximately constant due to competing effects of temperature and moisture.

4. Finally, at the end of the evening and during the night, the saturation pressure drops as the atmosphere and surface cool, and *VPD* decreases. As there is no more *PAR* available for photosynthesis, the plants keep their stomata closed to avoid water loss, resulting in negligible ET.

1.2.2. Mathematical Description

This section will give an overview of the equations that will be used for analysis, and introduce a simple ET-*VPD* model.

VPD [Pa] is a measure of the amount of water vapor the atmosphere is able absorb, and is defined as the difference between the saturated vapor pressure (e_{sat} [Pa]) and the atmospheric vapor pressure (e_a [Pa]) measured at the same level:

$$VPD = e_{sat} - e_a \tag{1.1}$$

where e_{sat} can be derived from temperature with the Clausius-Clapeyron relation.

ET is usually quantified as the latent heat flux L_vE where ET is abbreviated to E. The commonly used units for E of $mm\ day^{-1}$ are converted to $kg\ m^{-2}\ s^{-1}$ by use of the liquid water density ρ_w [kg m^{-3}]. L_v [J kg^{-1}] stands for the latent heat of evaporation. The total latent heat flux L_vE_{total} is generally made up by soil evaporation (L_vE_{soil}), evaporation of intercepted liquid water (L_vE_{liq}), and transpiration by the vegetation (L_vE_{veg}) (Van Heerwaarden, 2011).

Taking into account the relevant fractions (c_i [-]) of intercepted water and vegetation the equation for ET is:

$$L_vE_{total} = (1 - c_{veg})L_vE_{soil} + c_{veg}c_{liq}L_vE_{liq} + c_{veg}(1 - c_{liq})L_vE_{veg} \quad (1.2)$$

where the last term is dominant for fully vegetated surfaces. In modelling L_vE is often calculated by using the resistance expression (Moene and Van Dam, 2014):

$$L_vE = -\rho L_v \frac{q(z) - q_s}{r_a + r_s} \quad (1.3)$$

with ρ [kg m^{-3}] the air density, *q(z)* [kg kg^{-1}] the specific humidity at evaluation height *z*, and q_s [kg kg^{-1}] the specific humidity at the surface. r_a [s m^{-1}] is the aerodynamic resistance, which represents how well turbulence is able to exchange moisture, momentum, and heat between the surface and atmosphere. r_a is often parameterized as the the inverse of the effective wind speed (see Chapter 2.6.1). r_s [s m^{-1}] is the canopy resistance and is set by the trade-off of between CO_2 assimilation for photosynthesis and water loss, as described in Chapter 1.2.1.

From Equation 1.3 a conceptual model can be derived that explains the existence of ET-*VPD* hysteresis and its general tendencies. First, saturation at the surface is assumed, and the proportionality between the saturated vapor pressure and saturated specific humidity (q_{sat} [Pa])

$$q_{sat} \approx \frac{\epsilon e_{sat}}{P} \quad (1.4)$$

is used - and similarly that between atmospheric vapor pressure and specific humidity. ϵ = 0.622 is the ratio of the gas constants of dry air (R_d) and water vapor (R_v) and P [Pa] the pressure. Provided pressure differences are negligible - which is the case for typical evaluation heights - substituting in Equation 1.3 yields:

$$L_vE \propto \rho L_v \frac{e_{sat}(T_s) - e_a}{r_a + r_s} \quad (1.5)$$

with T_s [K] the surface temperature and e_a is taken at a set evaluation height (e.g. in case of the observations this would be the height of the EC setup and profile measurements used for further analysis). Equation 1.5 is equivalent to the expression used to calculate L_vE in second generation of atmospheric general circulation models (Sellers et al., 1997). When ρL_v is assumed constant during the day and the saturated vapor pressure for air (at the evaluation height) is inserted, the equation can be re-written as:

$$L_vE \propto \frac{e_{sat}(T_s) - e_{sat}(T_a)}{r_a + r_s} + \frac{e_{sat}(T_a) - e_a}{r_a + r_s} \quad (1.6)$$

where T_a [K] is the air temperature at the evaluation height, and $e_{sat}(T_a)$ - e_a the atmospheric *VPD* at that same height (Equation 1.1). Now $e_{sat}(T_s)$ can be expanded around T_a:

$$e_{sat}(T_s) \approx e_{sat}(T_a) + \frac{\partial e_{sat}}{\partial T}(T_s - T_a) \equiv e_{sat}(T_a) + s(T_s - T_a) \quad (1.7)$$

with s [Pa K^{-1}] the slope of the Clausius-Clapeyron relation at the evaluation temperature (here: T_a). Re-writing the first term of Equation 1.6 with this approximation gives

$$L_vE \propto \frac{s(T_s - T_a)}{r_a + r_s} + \frac{e_{sat}(T_a) - e_a}{r_a + r_s} \quad (1.8)$$

The temperature (T [K]) can be expressed as potential temperature (θ [K]):

$$\theta = T\left(\frac{P_0}{P}\right)^{\frac{R_d}{c_p}} \quad (1.9)$$

where P_0 [Pa] is a reference pressure, R_d [J kg^{-1} K^{-1}] the gas constants of dry air, and c_p [J K^{-1}] the heat capacity for water. The potential temperature can then be used to calculate the virtual potential temperature (θ_v [K]):

$$\theta_v = \theta(1 + 0.61q_v - q_l) \tag{1.10}$$

with q_v [kg kg^{-1}] the vapor content and q_l [kg kg^{-1}] the liquid water content. If only water vapor is present in the atmosphere, q_l is zero and q_v is identical to q.

If in Equation 1.9 P_0 is defined as the surface pressure $T_s = \theta_s$ holds, and we can crudely approximate $T_a \approx \theta_a \approx \bar{\theta}$ the potential temperature of the well-mixed BL. This approximation is justified by its limited impact, as also highlighted in Appendix A.3. The first term of Equation 1.8 now is proportional to H

$$H = \frac{\rho c_p}{r_a}(\theta_s - \bar{\theta}) \propto \frac{s(T_s - T_a)}{r_a} \tag{1.11}$$

As under the observational circumstances H is negligible with respect to L_vE (see Figure 3.2b for reference), the first term of Equation 1.8 can be neglected. Doing so yields the final equation for a conceptual model, which is akin to Dalton's law. Here ET is proportional to *VPD* (= e_{sat} - e_a) divided by the sum of the resistances:

$$L_vE \propto \frac{e_{sat}(T_a) - e_a}{r_a + r_s} \tag{1.12}$$

The ET-*VPD* hysteretic relationship follows from the model in Equation 1.12. This is illustrated by imposing typical diurnal courses for all variables. Under turbulent mixing r_a is assumed constant as the absolute wind speed is relatively constant for daytime conditions (Equation 2.17). For a well-watered surface in a temperate climate, in the morning the stomata are fully open and r_s can be assumed to be comparable in magnitude to r_a, whereas later in the day the stomata will close and r_s will rapidly increase to values far exceeding r_a. Under these conditions, *VPD* typically follows a semi-parabolic course,with a maximum in the second half of the afternoon.

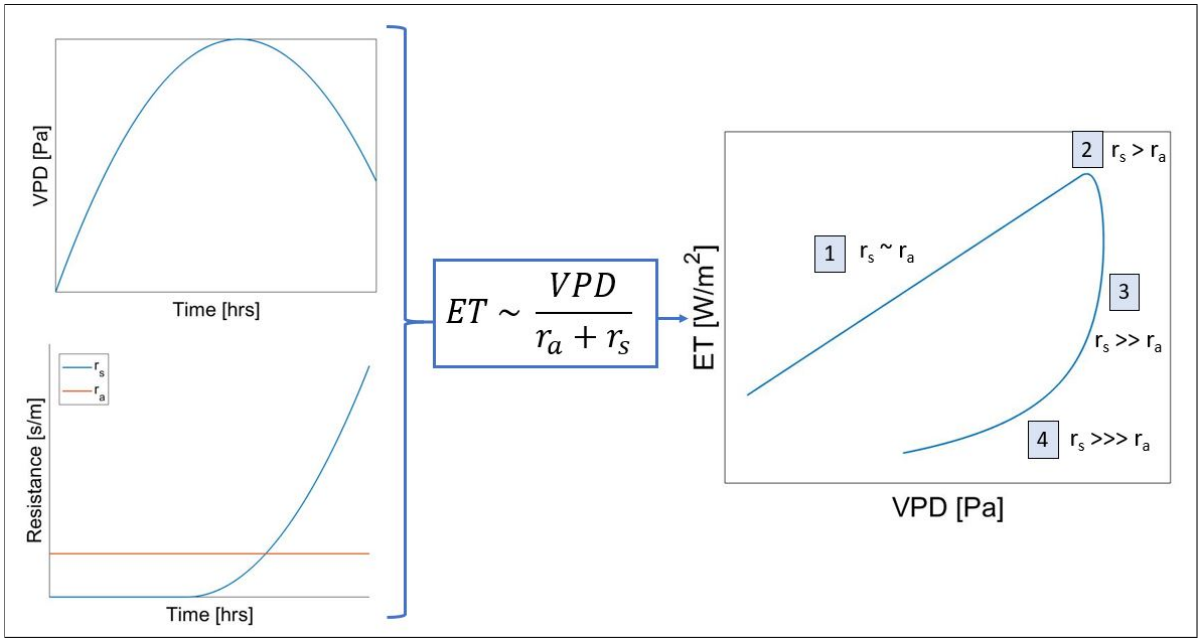

Figure 1.2: ET-*VPD* hysteresis explained with a conceptual model for ET, defined by Equation 1.12. Left: Typical diurnal curves for *VPD* and the resistances, where r_a is assumed constant; Right: Resulting hysteresis loop. 1-4 indicate the four regimes also identified in Figure 1.1 and described in Chapter 1.2.1. As r_a is assumed constant, the regimes can be related to the diurnal course of *VPD* and the relative magnitude of r_s with respect to r_a.

The diurnal courses of *VPD* and the resistances, as well as the resulting ET-*VPD* hysteresis are shown in Figure 1.2. The image illustrates how the diurnal course of *VPD* and relative magnitudes of r_s and r_a determine the overall behaviour of the ET-*VPD* hysteresis loop. Under constant r_a this behaviour sets the similar parameter regimes identified in Figure 1.1b; the regimes are described conceptually in Chapter 1.2.1. As the model is conceptual it has limited capability to reproduce all features: The horizontal plateau in Figure 1.1b (denoted with (2)) is for example reduced to a narrow zone due to the relatively rapid transition behaviour of r_s to high values. Furthermore, both modelling (Figure 3.7 in Chapter 3.2) and leaf level conductivity (not shown) reveal that the often used the assumption of constant values for r_a and morning r_s is broken under realistic conditions. And changes in the magnitude of r_a have a similar impact as those in r_s.

The principles of the conceptual model for ET can also be applied to analyse actual ET-*VPD* hysteresis, as illustrated in Figure 1.3. To do so, *VPD* is taken from the modelled case for 7 May 2018 (black curve; further described in Chapter 3.2). With this *VPD* and a representative value for r_a ET is calculated. If r_s is set in such a way that the initial slopes of the original and calculated curves match, the corresponding morning canopy resistance can be diagnosed. Then, considering the extreme limit where the stomata close instantaneously and r_s assumes a high value at once, the switching time for r_s is estimated, and the black curve is reduced to the red case. Here r_s initially is set to 50 s m^{-1}; at 15:00 r_s makes a discrete jump to a high value, simulated with 1000 s m^{-1}.

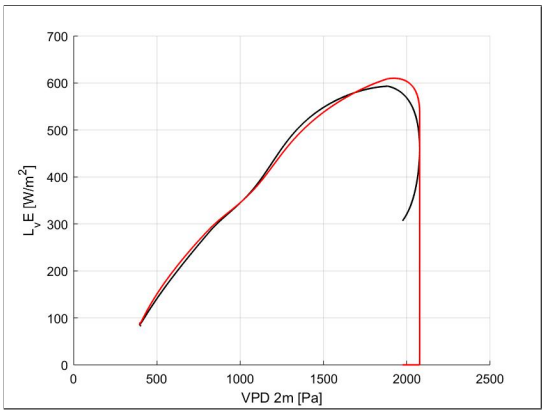

Figure 1.3: ET-*VPD* hysteresis. Black: Modelled curve for 7 May 2018, 8:00 - 16:30. Red: Curve reproduced with the conceptual model for ET, where *VPD* is taken from the black curve and r_a is set to 30 s m^{-1}; r_s transitions at 15:00 from 50 to 1000 s m^{-1}.

1.3. State-of-the-Art

1.3.1. Observations

The non-linear relation between vegetation behaviour and atmospheric conditions has been widely reported by for example Gutierrez et al. (1994) and Meinzer et al. (1995). Until the late 1990's work primarily focused on the relation between stomatal conductance (g_s [m s^{-1}]) and *VPD*. Takagi et al. (1998) for example describe that *"Plants may change the course of hysteresis of stomatal conductance according to the VPD maximum of the day"* and continue to explore the slope of the early morning g_s-*VPD* relation.

Canopy scale ET-*VPD* hysteresis was first reported by Doley in 1967, but not further investigated. More recently, several experimental studies on the ET-*VPD* hysteretic relationship and its possible causes were published (key publications in Table 1.1). Although these papers report the existence of the hysteretic relationship, a significant variability in loop characteristics is found; both between different studies and vegetation species, as well as on a seasonal and even day-to-day basis within single studies. Furthermore, there is no agreement between the reports on what induces the onset and shape characteristics of the hysteresis. Different possible causes are named, ranging from soil moisture availability to atmospheric conditions to vegetation state, whereas sometimes no clear cause could be determined.

The diversity in observational findings suggests that there is an interplay of processes at work: The dominant driver of ET-*VPD* hysteresis differs depending on surface specifics and the BL's competing processes and their feedbacks. Thus the papers point at environmental and BL conditions as well as vegetation species and state, without pinpointing why the identified variables are found to control the ET-*VPD* hysteresis.

Paper	**Climate**	**Method**	**Instrument**	**Identified Concepts**
Doley(1967)	Temperate forest	Leaf rapid weighing and stem sap flow on 1 tree species	Scale and heat pulse velocity	Leaf, stem, and root storage
O'Brien et al. (2004)	Wet tropical forest	Xylem sap flow on 10 tree species	Thermal dissipation probe	(Species)
Zeppel et al. (2004)	Temperate forest	Xylem and stem sap flow on 4 tree species	Heat pulse velocity	(Species, season)
Ewers et al. (2005)	Boreal forest	Stem sap flow on 1 tree species	Thermal dissipation probe	(Species, age)
Wullschleger et al. (1998)	Temperate forest	Stem sap flow on 1 tree species	Not clear	Soil moisture
Meinzer et al. (1999)	Temperate forest	Stem sap flow on 4 tree species	Thermal dissipation probe	(Species, season)
Chen et al. (2011)	Temperate urban environment	Stem sap flow on 3 tree species	Thermal dissipation probe	*VPD*
O'Grady et al. (1999 & 2008)	Temperate forest	Leaf sap flow on 1 tree species	Heat pulse velocity	*VPD*, not soil moisture
Unsworth et al. (2004)	Temperate forest	Xylem and stem sap flow on 1 tree species, water vapor flux	Heat pulse probe, EC	plant water potential; hydraulic capacitance
Zhang et al. (2014)	Temperate meadow in forest	Water vapor flux on mixed species	EC	time lag between *PAR* and *VPD*; root, leaf, and soil water potential
Zheng et al. (2014)	Alpine shrub land	Water vapor flux on mixed species	EC	Time lag between *Q** or T_a and *VPD*, plants stress, water availability

Table 1.1: Key papers reporting ET-*VPD* hysteresis: Summary of measurement site, method, and suggested factors driving ET-*VPD* hysteresis. Factors in brackets have been reported without being identified as main driving variables.

1.3.2. Modelling

Only two studies have been published that attempt to explain the mechanisms driving ET-*VPD* hysteresis with modelling. Tuzet et al. (2003) adapt a mechanistic soil–plant–atmosphere continuum model from Leuning (1995) and force it with idealized diurnal courses of radiation, temperature, wind speed, and pressure. Their model result shows a hysteretic relationships of ET with leaf level *VPD*. Although the model manages to capture hysteresis occurrence, its shape is unrealistic with respect to observed hysteresis loops.

More recently Zhang et al. (2014) have combined observations with modelling to develop a theoretical framework to specifically investigate the causes for the existence and magnitude of the ET-*VPD* hysteresis. Their analysis consists of four models:

1. A model that assumes the time difference between the diurnal maximum net radiation (Q^* [W m^{-2}]) and maximum *VPD* as the driver. This time lag is used to fit a theoretical ellipse to the data, in order to explain the occurrence of the hysteresis.
2. A soil moisture storage model to show that this storage also leads to hysteresis, albeit transient in nature and only occurring if the soil moisture is below a certain threshold level.
3. A diagnostic soil-plant-atmosphere continuum (SPAC) model forced with representative values for Q^*, the ground heat flux (G [W m^{-2}]), air temperature, and absolute wind speed (U [m s^{-1}]) - to explain how hysteresis is impacted by the Q^*-*VPD* lag, soil moisture stress, and internal plant water status.
4. An altered (diagnostic) SPAC model that includes plant hydraulic capacitance to shows that imposing higher root to leaf hydraulic capacities (at 8000 mmol m^{-2} MPa^{-1}; ten times that of grass) in itself also results in hysteresis.

Based on their theoretical assessment and comparison with experimental data, Zhang et al. (2014) conclude that the time lag between *PAR* (or Q^*) and *VPD* causes the onset of the observed ET-*VPD* hysteresis, whereas its magnitude is influenced by root, leaf, and soil water potentials. As the plant potentials are in turn linked to soil moisture availability and hydraulic capacitance, Zhang et al. (2014) therefore confirm the impact of all factors identified by the papers in Table 1.1 on ET-*VPD* hysteresis.

In spite of the significant progress in understanding the drivers of ET-*VPD* hysteresis, the theoretical foundation of Zhang et al. (2014) is unable to explain the relative importance of identified concepts in setting the diurnal ET-*VPD* course. Furthermore their SPAC model is diagnostic as it is forced with the very quantities that define most of the diurnal course of the BL (e.g. *VPD*, Q^*, ground heat flux, air temperature, and a representative value for wind speed. Thus inhibiting the feedback mechanisms - via e.g. exchange of water vapor, heat, and momentum between the BL and the underlying surface - between ET and the forced quantities. In addition, their model does not incorporate large-scale BL dynamics such as entrainment, that may affect ET-*VPD* hysteresis loops via exchange of heat and moisture at the BL top.

1.4. Knowledge Gap and Problem Statement

Already in 1967 Doley reports: *"In spring, the daily course [of the sap flux - water deficit relationship; edit] resembled a hysteresis loop of large capacity."* In spite of recent experimental efforts, it still remains unclear what mechanisms are dominant in driving the variations in diurnal ET-*VPD* hysteresis. Due to the complexity of interacting processes whose impact varies depending on the atmospheric and surface conditions, it remains highly unlikely that experimental work alone will conclusively unravel all drivers of ET-*VPD* hysteresis.

No simple prognostic model is currently able to capture ET-*VPD* hysteresis realistically. Tuzet et al. (2003) use a diagnostic model with a mechanistic parameterization of the stomatal behaviour to show the impact of soil moisture stress on hysteresis. However, the shapes

of their ET-*VPD* hysteresis loops are unrealistic, as they have never been confirmed experimentally. Zhang et al. (2014) have explored modelling the soil–plant–atmosphere continuum by forcing several radiation and atmospheric variables, and manage to model the experimentally observed hysteresis loops. Although their result furthers the understanding of ET-*VPD* hysteresis, their approach also is diagnostic and therefore inhibits the two way interaction between surface and atmosphere. Nor does it incorporate a mechanistic description of the stomatal trade-off between CO_2 capture and water loss in setting ET. Therefore impeding key feedbacks. Furthermore, neither model allows for large-scale BL dynamics such as entrainment and advection of moisture and heat - which most likely influence the occurrence of ET-*VPD* hysteresis, as pointed out in the discussion of Zhang et al. (2014).

In summary, it remains unclear how diurnal ET-*VPD* hysteresis is shaped. Thorough analysis requires continuous multi-year and multi-scale data sets that span biology, hydrology, and meteorology; where its results will only apply to the specific study site. Alternatively, modelling may be a powerful and complementary tool to integrate data sets and demonstrate the sensitivity of the ET-*VPD* hysteresis to the state of the atmosphere, vegetation, and soil. However, to this date no prognostic model that couples surface and atmosphere as well as incorporates vegetation biology has been able to realistically reproduce ET-*VPD* hysteresis, including all its underlying feedback mechanisms.

1.5. Objectives

To bridge the knowledge gap in unraveling the drivers of ET-*VPD* hysteresis and contribute to an improved understanding of ET, this thesis aims to combine a comprehensive set of observations with prognostic modelling. In this manner we will investigate how the shape of the ET-*VPD* hysteresis loop is influenced by the state the vegetated surface as well as large-scale BL processes such as subsidence and entrainment. The data set captures biological, hydrological, and meteorological variables, and incorporates all scales of influence, from leaf to BL. In addition, for the first time a prognostic model will be used to take into account the non-linear feedback mechanisms associated with the dynamics of a coupled soil-vegetation-atmosphere system. Furthermore, the model's biology-based mechanistic representation of vegetation will allow for investigation of the impact of various drivers on the vegetation's ability to transpire, and consequently on the hysteretic behaviour.

Research Question:

> **Can the characteristics of ET-*VPD* hysteresis uncover and quantify the contributions of surface and atmospheric processes in controlling ET?**

Our strategy to answer the research question is to:

1. Analyse observations from the 2018 CloudRoots campaign to identify what ET-*VPD* hysteresis shapes occur and, to disentangle different shapes according to their distinct drivers.
2. For the first time give a proof-of-concept for modelling ET-*VPD* hysteresis with a prognostic model that incorporates surface-BL feedbacks, large-scale BL dynamics, and a mechanistic vegetation model derived from biology.
3. Deliver an observation inspired reference case, and perform a sensitivity study to systematically analyse the impact of changes in vegetation state, BL state, and synoptic forcing on ET-*VPD* hysteresis.

By doing so, this study will combine observations with modelling and integrate knowledge from meteorology, hydrology, and biology, to cross the scales from the leaf to the BL. For

the first time a proof-of-concept will be given for realistically modelling ET-*VPD* hysteresis in a prognostic model that captures both vegetation mechanisms and atmosphere-surface feedbacks. Therefore allowing for a new way of studying how processes control ET, and improving the understanding of ET. This will lead to a better representation of ET in models, and subsequently better weather, climate, and soil moisture availability forecasts.

Beyond the scope of this project, the ultimate goal is to derive typical surface and atmospheric characteristics by analysing a *single* hysteresis loop. Within this long-term framework, this thesis aims to contribute the basis for further sensitivity studies and offer a means of interpreting them.

2

Methodology

This chapter describes the overall research approach (Chapter 2.1). First we discuss the measurement site (Chapter 2.2) and its heterogeneity (Chapter 2.3). Next the available observations (Chapter 2.4), and selection of the reference case (Chapter 2.5). Chapter 2.6 introduces the ML model and its essential assumptions and equations. Last, the sensitivity analysis is defined (Chapter 2.7).

.

2.1. Approach

To answer the research question whether ET-*VPD* hysteresis can help disentangle surface and large-scale processes in controlling ET, and quantify their contributions, observations are combined with modelling. The steps in the research strategy as shown in Figure 2.1 are:

1. The observed ET-*VPD* curves (Figure 1.1a) are inspected to determine what metrics are appropriate to characterise hysteresis shape. A representative day - in terms of cloud conditions, past precipitation, and daytime turbulent mixing - is selected for modelling. For this day the early morning variables for soil, surface, BL, and lower troposphere are determined for further modelling.

2. The selected day is modelled in a coupled prognostic Mixed-Layer (ML) model containing a mechanistic vegetation parameterization. The results are validated against the observations to give a proof-of-concept for the proposed modelling approach.

3. The proof-of-concept case is simplified to a reference case, that is used to perform a sensitivity study. The study analyses how the hysteresis responds to changes at the surface (soil moisture, vegetation capacity to assimilate CO_2 for photosynthesis), to large-scale BL (entrainment) and synoptic (subsidence) processes, and to turbulent mixing.

2.2. Site Description

The experimental data is part of the multi-disciplinary CloudRoots field campaign, financially supported by TransRegio project TR32. It was collected from May to August 2018 at the Integrated Carbon Observation Site (ICOS) near Selhausen, Germany (site code: DE-RuS). The site lies at 50.9 °N, 6.5 °E, at 104.5 meters above sea level and is part of the lower Rhine basin. It lies within 10 km from the Jülich Observatory for Cloud Evolution (JOYCE; 50.1°N, 6.2°E), and about 100 km from the radiosonde site near Essen. Local time during the campaign is UTC+2.

The area's climate is temperate with year round precipitation typically ranging from 53 to 81 mm per month and average 24-hour temperatures ranging from 2 to 18 °C (Climate-data.org, 2019). The soil is silt-loam, with an average of 14% clay, 73% silt, and 13% sand content and a pore volume fraction of 0.353. The soil moisture is near field capacity[1].

The field is planted with winter wheat, which has a *C3* photosynthesis pathway (description in Vilà et al., 2015). At the start of the observational period, the vegetation almost fully covers the underlying soil and is about 0.45 m high; maximum crop height is 0.7-0.8 m at the end of the campaign. The root zone extends from the surface to a depth of 3 m, and senescence starts in mid-June.

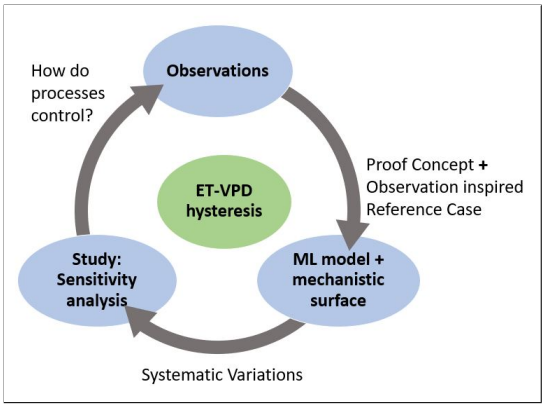

Figure 2.1: Schematic depiction of the project setup. The blue ovals represent the three key research steps; the text next to the arrows the desired output of each step.

Figure 2.2a shows the area surrounding the site is heterogeneous, featuring villages, roads, trees, other agricultural crops (sugar beet, winter barley, maize, and rape seed), and two substantial brown coal mines. Heterogeneity exists at multiple scales - a schematic depiction of the length scales that influence the measurements is given in Figure 2.2b - and adds complexity: The BL dynamics above blending height are not representative for the measurement site alone but are an interplay of all landscape contributions. Thus impacting measured fluxes, and surface and BL variables. To investigate the diurnal evolution of quantities as ET and *VPD*, this large scale heterogeneity must be taken into account (Chapter 2.4).

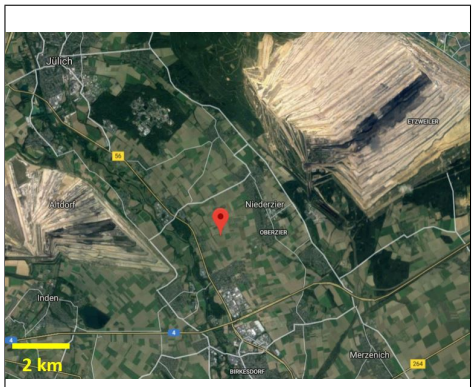

(a) Satellite

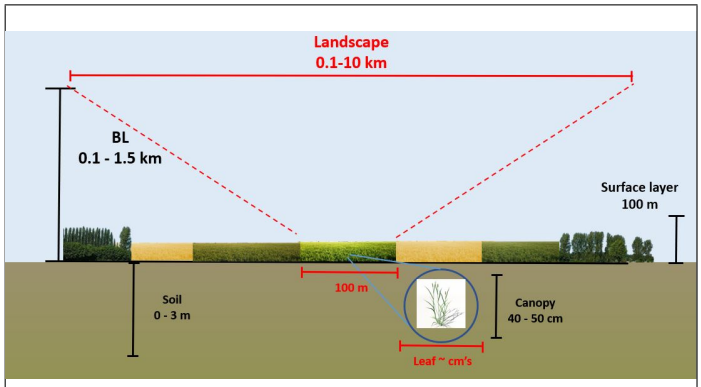

(b) Length scales at play

Figure 2.2: Measurment site: (a) Satellite image of the site and its surroundings; (b) Schematic depiction of horizontal (red) and vertical (black) scales influencing the measurements. In Figure b the horizontal 100 m scale depicts the site of the CLoudRoots experiment, whereas the horizontal 0.1-10 km scale shows the landscape contribution to driving BL evolution above the field.

2.3. Measurements

The CloudRoots field campaign consists of a large number of parallel hydrological and meteorological measurements. During intensive observation periods (IOPs) also leaf level biology is investigated. Thus covering the full range of scales from leaf to BL and lower troposphere. The relevant data sets are discussed below, and an overview is given in Table 2.1. All data is open access and has been archived in the Transregio database (`http://www.tr32db.uni-koeln.de`).

[1] volume fraction of water after saturation, where water has been allowed to drain freely due to gravity.

Available data for	Frequency	Measurements from	Variables
Vegetation biology	Hour; on IOPs	Leaf level gas exchange	mesophyll conductance (g_m [m s^{-1}]), CO_2 maximum primary production ($A_{m,max}$[mg m^{-2} s^{-1}]), Initial low light conditions use efficiency for CO_2 (α_0 [mg J^{-1}])
Canopy cover	Week	Manual	*LAI*, canopy height
Field fluxes & 2 m values	Half hour	EC	L_vE, *H, q, T, P, u,* CO_2
In- and near-canopy	Seconds	Profile measurements 0 - 2 m	*q, T, u,* CO_2
Soil	Minute	Soil measurements at 0.01 - 1 m	soil moisture, *T, G*
Radiation	Seconds	Radiometer	Incoming and outgoing short & long-wave radiation (S_{in}, S_{out}, L_{in}, S_{out} [W m^{-2}]), *PAR*, albedo (α [-])
BL & above	5 min	Cloud radar, microwave	BL height, *T, u*, precipitation
BL & above	12 hours	Radiosonde	Inversion strength & free troposphere lapse rate for *q, T*
Weather conditions	Daily	Weather maps	Pressure
Weather conditions	< seconds	Camera	Clouds, precipitation

Table 2.1: CloudRoots data set: Available observations, frequency, and measured variables.

Over the period from May to July 2018 there is a continuous setup of the EC at 1.93 m height (SN1185 Irgason EC150 system, Campbell Sci; PTB101B pressure sensor, Vaisala) with sonic anemometer (CSAT3), from which the 30-minute averaged data is used. Also radiation (CM14 for global and CG2 for long wave radiation, Kipp & Zn), ground heat flux and temperatures (SHFP CR1000, Hukseflux; at 1, 5, 10, 20, 50, and 100 cm deep), PAR (Kipp & Zn), soil moisture (Campbell Sci, CS616) are measured.

During IOPs on 7-8 May, 15 June, and 28 June leaf gas exchange measurements are performed (LI-6400XT, Li-Cor). In addition a novel 0-2 m profile setup as described by Ney et al. (2018) is in operation to measure temperature, humidity, CO_2 concentration, and wind speed (LI-7000, Li-Cor Biosciences for gas concentrations; FW3 thermocouple Campbell Scientific for temperature; 8455-075-1, TSI for wind), from which the 30-minute averaged data is used.

Large scale boundary layer and lower free troposphere (FT) characterisation are provided by radiosonde measurements in Essen (Temperature and specific humidity; at 0:00 and 12:00) and the JOYCE facility (cloud radars JOYRAD-35 and JOYRAD-94, microwave HATPRO-TOPHAT, Atmospheric Emitted Radiance Interferometer (AERI), ceilometer CT25K, micro rain radar).

2.4. Incorporating Heterogeneity

The model used in this study (Chapter 2.6) assumes horizontal homogeneity at the surface over kilometer length scales and vertical homogeneity in the canopy and soil. To incorporate landscape heterogeneity (Figure 2.2) the following research strategy is employed:

- **Small scale heterogeneity**: Transpiration differs depending on where the stomata are positioned on the leaf and whether the stomata are covered in water film. On a slightly

larger scale the canopy layer is both horizontally and vertically heterogeneous in terms of leaf density. As the light intensity decreases with depth in the canopy, *PAR* intensity also decreases. Hence biochemical reaction rates differ along the depth of the canopy due *PAR*, temperature, specific humidity, and CO_2 gradients within. This spacial variation is accounted for by assuming a typical leave distribution over the vertical. Furthermore, skin temperature, specific humidity, CO_2 concentration, and the fraction of intercepted water are assumed constant over the canopy depth. The attenuation of *PAR* is incorporated by integrating over a leaf area index (*LAI* [-]) based ensemble of sunlit and shaded leaves (Jacobs and De Bruin, 1997; Pedruzo-Bagazgoitia, 2015).

- **In-field scale**: Surface heterogeneity at the field due to vegetation cover and LAI variations are neglected; as are the presence of the measurement setup and the impact of underlying paleo-rivers (Von Hebel et al., 2018).
- **Field scale**: The area surrounding the field consists of a mosaic of surface types. All these different types result in their respective ET and *H*. ET is a local variable that represents the state of the surface, and directly corresponds to the measured biological state of the vegetation, soil moisture, *VPD*, *T*, *PAR*, and CO_2 concentration. Therefore the ET observed over the measurement site will directly be used as the representative value - in contrast to *H*, which is strongly impacted by large scale advection (see below).
- **Boundary layer scale**: *H*, on the other hand, is a variable that is influenced by the entire landscape. Each surface type produces its own *H*, which dominates the corresponding buoyancy flux. As the distance above the surface increases, the fluxes of the measurement site and surrounding fields mingle progressively. And above the blending height, their combined impact sets the rate of BL growth and ML temperature evolution - as confirmed by the uniformity of the BL height measured by JOYCE and the radiosonde (Chapter 2.3). The *H* measured at the field itself however, is proportional to the difference between surface and ML temperature (Equation 1.11), and is directly influenced by the landscape contributions. Resulting in an negative *H* at the measurement site for warm, sunny days. To incorporate the landscape scale impact of *H* on temperature evolution and BL growth in the model, the modelled *H* is allowed to be in line with the landscape average. This is done by advecting heat (further specified in Appendix B), corresponding to the temperature contrast between the study site and surroundings. To do so the flux of a neighbouring field with bare soil is used as a proxy for the aggregated landscape *H*.

2.5. Case Selection

To give a proof-of-concept for the modelling approach, and to create a reference case for further sensitivity analysis, a reference diurnal ET-*VPD* hysteresis loop is selected from all suitable loops (Figure 1.1a). The applied filtering is based on:

- Vegetation state: Full photosynthesis;
- Meteorological conditions: Clear skies and low winds;
- To avoid the contributions of intercepted rain water to ET: Absence of precipitation for at least two days;
- Completeness and quality of the data set: Intensive Observation Period preference.

Based on the criteria above, 7 May 2018 appears to be the most suitable day for further analysis. In addition, to fulfill the ML model's mixed condition the selected day must be a convective case. This condition is confirmed by inspection of the integrated water vapor column, where minute scale fluctuations indicate entrainment of dry air.

7 May 2018 was a day with clear skies and no clouds. In the early morning dew was observed on the vegetation. The air was warm with the 6:00 near-surface temperature already

reaching 13 °C, and a maximum 2 m temperature of 24 °C around 16:00. The air was relatively dry with a typical specific humidity of 7 g/kg at 2 m. The combination of low specific humidity with high temperatures leads to a day with high overall *VPD* values. Winds are weak, coming from the south-east, with a maximum wind speed of just under 2.5 m s^{-1} between 09:00 and 11:00. The vertical wind speed is about 1% of the horizontal. BL height measurements from the radiosonde and JOYCE ceilometer show a homogeneous profile over a 100 km distance range. The weather map shows that the study site is halfway between the adjacent high and low pressure regions. The residual for the energy budget (Q^* - G - L_vE - H) is approximately 100 W m^{-2}; both due to underestimation of the measured L_vE (Wang et al., 2012; Malek, 1993) and to heat advection due to landscape heterogeneity (Stoy et al., 2013; case description in Chapter 2.4).

2.6. Model

To prognostically model the diurnal variability of ET-*VPD* hysteresis the CLASS ML model (Vilà et al., 2015) is used; it is schematically depicted in Figure 2.3. ML modelling has been proven instrumental as it incorporates essential physical processes, which a more simplistic model might miss or more complex model obscure. Furthermore, the embedded mechanistic A-r_s model (Chapter 2.6.2) for canopy resistance allows for a biology-based representation of the stomata's behaviour, rather than the often used semi-empirical parameterizations.

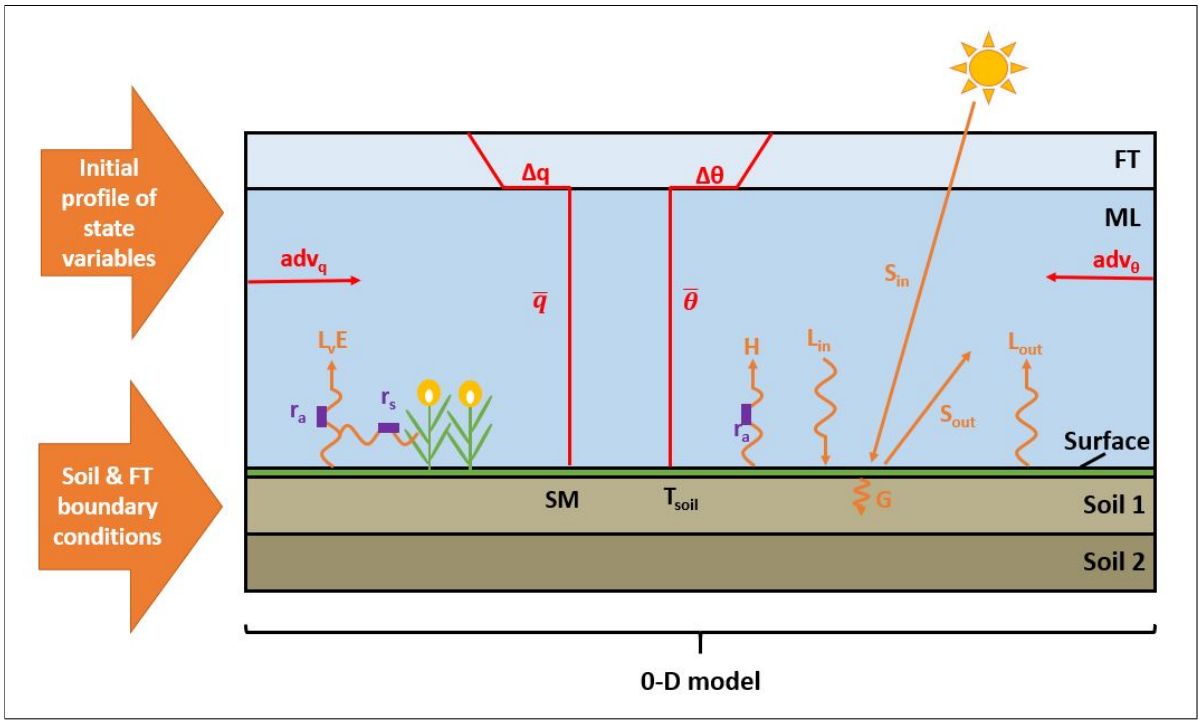

Figure 2.3: Schematic depiction of the CLASS ML model. The radiative and turbulent heat fluxes are depicted in orange; The profile of ML and FT variables, and the advection thereof (adv_q for q and adv_θ for θ), in red; Resistances are shown in purple. The figure is inspired by work from Van Heerwaarden (2011).

The model consists of five virtually interconnected 0-D boxes, that have no z-coordinate and assume horizontal homogeneity for all variables. It uses the assumption that convective turbulence mixes the air within the daytime BL well, to describe the diurnal evolution of variables in the convective ML. The key components of the model are:

1. The incoming solar **radiation** (S_{in}) is calculated based on latitude, longitude, day of the year, and time of the day. A constant albedo sets the reflected amount (S_{out}). L_{in} and L_{out} are calculated with the Stefan-Boltzmann law, where the surface and atmospheric

emissivities are respectively set to 1 and 0.8, and the atmospheric temperature from the top of the surface layer is used.

2. The **Soil** consist of an upper layer where the diurnal cycle is felt, and a deeper soil layer where temperature and soil moisture remain constant. The temperature and soil moisture content are parameterized with a force-restore model.

3. At the **surface** the net radiation Q^* (= S_{in} - S_{out} + L_{in} - L_{out}) is partly absorbed by the soil as ground heat flux (G); the remaining available energy is partitioned into L_vE and H. Heat, moisture, and atmospheric constituents have separate (atmospheric) surface values, which amongst others depend on the turbulent fluxes and typically differ from their ML value. In addition the surface variables determine the stomatal response, which is calculated in a separate A-r_s model component (described further in Chapter 2.6.2).

4. The model only considers turbulent fluxes at the bottom and top of the **ML**, which are a consequence of its two evolving boundaries: The surface and FT. In addition heat, moisture, and constituents may advect into the ML; within the ML heat, moisture, and constituents are assumed to be uniform with height. The ML values evolve according to the equations set out in Chapter 2.6.1.

5. The **FT** lies at the top of the ML, separated by an infinitely shallow inversion layer which is parameterized by a discrete jump for $\bar{q}$ (Δq) and $\bar{\theta}$ ($\Delta\theta$). Dry air and heat from the FT are entrained into the ML. These entrainment fluxes are determined by the entrainment velocity (w_e [m s^{-1}]) and the magnitude of the jump. The lapse rates γ_q and γ_θ remain constant, whereas the jumps change depending on the entrainment rate. The effects of subsidence and radiation on FT specific humidity and temperature evolution are neglected.

6. The diurnal evolution of the ML **wind** is calculated similarly to $\bar{\theta}$ and $\bar{q}$, with momentum entrainment from the FT and assuming that the FT is in geostrophic equilibrium.

7. The model contains a **surface layer** (SL) which is defined as the lowest 10% of the ML. Here, the differences between ML and surface values are interpolated by means of the aerodynamic mixing - which is determined from wind and atmospheric stability. Therefore allowing for evaluation of e.g. 2 m values.

In coupled mode adjacent layers interact every iteration, allowing model quantities to evolve according to the soil, surface, and BL processes, horizontal advection of heat and moisture, and the FT state. The model is initialized at 6:00, when the BL fulfills the well-mixed condition and in-canopy gradients for temperature and specific humidity are small. The initial and boundary conditions are set, and the model is left to iterate without intervention until 16:30. After 16:30 the assumption of a fully convective ML does not hold for several of the sensitivity analysis cases. For the reference case the ML is convective until 16:52 (Figure 3.3); however for consistency the model is stopped at 16:30 as well.

A full description of the model components is given by Van Heerwaarden (2011) and Vilà et al. (2015).

2.6.1. Model Equations

The evolution of the ML height h [m], $\bar{q}$, $\bar{\theta}$, and winds $\bar{u}$ and $\bar{v}$ are described by a set of equations and is based on the work of Lilly (1968) and Tennekes (1973). Here w_s, advection, and turbulent heat fluxes are taken as external forcing. The full derivation of all equations is described by Vilà et al. (2015).

The ML height grows as:

$$\frac{\partial h}{\partial t} = w_e + w_s \tag{2.1}$$

where w_e [m s^{-1}] is the entrainment velocity and w_s [m s^{-1}] the mean vertical subsidence velocity. w_s is positive in the upward direction, and is calculated from large-scale wind divergence (*div(U)* [s^{-1}]) by

$$w_s = -\mathrm{div}(U)h \tag{2.2}$$

w_e is calculated as:

$$w_e = \frac{\overline{(w'\theta_v')_e}}{\Delta\theta_v} + \frac{5u_*^3\theta_v}{\Delta\theta_v} = \frac{A\overline{(w'\theta_v')_s}}{\Delta\theta_v} + \frac{5u_*^3\theta_v}{\Delta\theta_v} \tag{2.3}$$

where the first term represents the flux contribution to the entrainment velocity, and the second the - generally much smaller - contribution from wind shear. $\overline{(w'\theta_v')_s}$ [K m s^{-1}] and $\overline{(w'\theta_v')_e}$ [K m s^{-1}] respectively are the surface and entrainment kinematic buoyancy fluxes; where the surface flux is the dominant driver of BL mixing and growth (Stull, 1998). A [-] is the ratio between the fluxes, and is generally set to 0.2 $\Delta\theta_v$ is the jump of θ_v at the top of the ML, and u_* the friction velocity. As q generally is small (orders of magnitudes smaller than 1), $\overline{w'\theta_v'}$ can be calculated from its heat and humidity contributions (Stull, 1988) as:

$$\overline{w'\theta_v'} = \overline{w'\theta'} + \overline{\theta_v}\left(\frac{R_v}{R_d} - 1\right)\overline{w'q'} = \frac{H}{\rho c_p} + 0.61\overline{\theta_v}\frac{L_v E}{\rho L_v} \tag{2.4}$$

with $\overline{w'\theta'}$ the kinematic heat flux and $\overline{w'q'}$ the kinematic moisture flux.

The mixed layer potential temperature $\bar{\theta}$ and its jump at the ML top evolve as:

$$\frac{\partial\bar{\theta}}{\partial t} = \frac{1}{h}\left(\frac{H}{\rho c_p} + w_e\Delta\theta\right) + adv_\theta \tag{2.5}$$

$$\frac{\partial\Delta\theta}{\partial t} = \gamma_\theta w_e - \frac{\partial\bar{\theta}}{\partial t} \tag{2.6}$$

with adv_θ the lateral advection of heat into the ML (Figure 2.3).

Mixed layer specific humidity $\bar{q}$ and its jump evolve as:

$$\frac{\partial\bar{q}}{\partial t} = \frac{1}{h}\left(\frac{L_v E}{\rho L_v} + w_e\Delta q\right) + adv_q \tag{2.7}$$

$$\frac{\partial\Delta q}{\partial t} = \gamma_q w_e - \frac{\partial\bar{q}}{\partial t} \tag{2.8}$$

with adv_q the lateral advection of specific humidity into the ML (Figure 2.3).

The zonal mixed layer wind $\bar{u}$ and its jump Δu evolve as:

$$\frac{\partial\bar{u}}{\partial t} = -f_c\Delta v + \frac{1}{h}(\overline{u'w'} + w_e\Delta u) + adv_u \tag{2.9}$$

$$\frac{\partial\Delta u}{\partial t} = \gamma_u w_e - \frac{\partial\bar{u}}{\partial t} \tag{2.10}$$

with f_c the Coriolis force, $\overline{u'w'}$ the turbulent momentum flux for u, adv_u the lateral advection of u into the M, and γ_u the FT lapse rate for u. Δu is defined as the difference between the geostrophic wind and mixed layer wind in the zonal direction, where the wind velocity in the FT is assumed to be equal to the geostrophic wind at that height.

The meridional mixed layer wind $\bar{v}$ and its jump evolve as:

$$\frac{\partial\bar{v}}{\partial t} = f_c\Delta u + \frac{1}{h}(\overline{v'w'} + w_e\Delta v) + adv_v \tag{2.11}$$

$$\frac{\partial\Delta v}{\partial t} = \gamma_v w_e - \frac{\partial\bar{v}}{\partial t} \tag{2.12}$$

with $\overline{v'w'}$ the turbulent momentum flux for v, adv_v the lateral advection of v into the M, and γ_v the FT lapse rate for v. Similar to the zonal wind, Δv is defined as the difference between the geostrophic wind and mixed layer wind in the meridional direction.

As w_e (appearing in Equations 2.1, 2.6, 2.8, 2.9, and 2.11) is also determined by H and L_vE (Equation 2.3), the diurnal evolution of ML values and BL growth are primarily driven by the sensible and latent heat flux. In turn they are linked by the surface energy partitioning of available energy:

$$Q * -G = L_vE + H \tag{2.13}$$

where H is given by Equation 1.11, and the three contributions to ET (introduced in equation 1.2) are respectively parameterized as:

$$L_vE_{liq} = \frac{\rho L_v}{r_a}(q_{sat}(T_s) - \bar{q}) \tag{2.14}$$

$$L_vE_{soil} = \frac{\rho L_v}{r_a + r_{soil}}(q_{sat}(T_s) - \bar{q}) \tag{2.15}$$

$$L_vE_{veg} = \frac{\rho L_v}{r_a + r_s}(q_{sat}(T_s) - \bar{q}) \tag{2.16}$$

where r_s is set by the mechanistic model for vegetation transpiration (Chapter 2.6.2), the soil resistance for evaporation r_{soil} [s m^{-1}] by a minimum resistance and moisture availability function (*f(w)* [-]), and r_a by

$$r_a = \frac{1}{C_sU} \tag{2.17}$$

with C_s the drag coefficient for scalars, which is in turn related to atmospheric stability, surface layer height, and the vegetation height via the roughness lengths for momentum and heat. *f(w)* is a fraction [-] in the range between 1 (no soil moisture stress) and 0 (full stress). The intermediate step function has a linear profile between the wilting point (w_{wilt} [-]) and field capacity (w_{fc} [-]):

$$f(w) = \frac{w_2 - w_{wilt}}{w_{fc} - w_{wilt}} \tag{2.18}$$

with w_2 [-] the soil moisture content of the lower layer.

For the work presented in this study, the model is updated by including the morning transition from residual layer (RL) to FT, by improving the parameterization for the leaf level vapor pressure, and by improving the surface layer temperature and pressure parameterizations. The changes are described in Appendix A.

2.6.2. Mechanistic A-r_s Model for Vegetation Transpiration

The mechanistic *A*-r_s model determines the vegetation's ability to transpire, by using the rate of CO_2 uptake (A [mg m^{-2} s^{-1}]) to calculate the vegetation resistance for water vapor release (r_s). It is also know as the *A*-g_s model, where g_s stands for either the stomatal or canopy conductance. The model is based on the trade-off between the benefits of CO_2 capture and detriments of water loss, as described in chapter 1.2.1. The model equation and parameters depend on vegetation biology, following the approach described by Goudriaan (1986), Jacobs et al. (1996), and Ronda et al. (2001).

The canopy resistance is made up by the virtual ensemble of individual stomatal resistances. Each stomatal resistance is in turn a resultant of the resistances for gas exchange between (1) the atmosphere and stomatal cavity (depending on the vapor pressure and CO_2 gradients between the stomatal cavity and the surrounding atmosphere), (2) the stomatal cavity and mesophyll, and (3) the atmosphere and inner leaf via the cuticle (Figure 2.4). As

described in Chapter 1.2.1, the stomata adjust their aperture in response to the availability of *PAR*, leaf level *VPD*, surface temperature , and soil moisture. Thus setting the diurnal course of r_s.

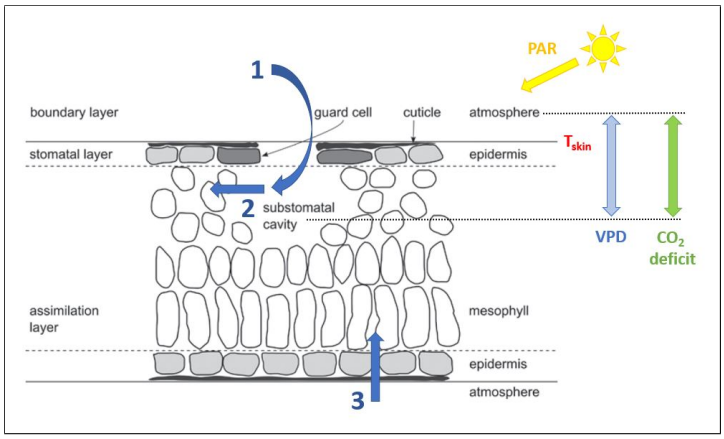

Figure 2.4: Schematic depiction of a leaf cross-section with the atmospheric drivers of stomatal aperture. The three components making up the effective resistance of the stomata are: 1. Resistance for gas exchange from the atmosphere to the substomatal cavity; 2. Resistance for transport from the cavity into the mesophyll; 3. Resistance for cuticular gas exchange. Figure adapted from Moene and Van Dam (2014).

The model assumes leaf level *VPD*, surface temperature, and CO_2 deficit between leaf and atmosphere to remain constant within the entire depth of the canopy layer. This is a key simplification with respect to the observed gradients and literature (Jarvis and McNaughton, 1986), and ignores that the vegetation itself is a source of water vapor and that evaporation reduces the local leaf temperature. In addition, the response to the availability of *PAR* is incorporated by a mathematical integration over an ensemble of shaded and sunlit leaves (Jacobs and De Bruin, 1997; Pedruzo-Bagazgoitia, 2015). The vapor pressure within the stomata is assumed to be at saturation point. The sensitivity of the vegetation to soil moisture stress is incorporated via the linear water availability function *f(w)*, as discussed in Chapter 2.6.1. The choice of stress function is one of the major modelling uncertainties for r_s and consequently ET (Combe et al, 2016). However, as the reference case is under field capacity conditions and soil moisture stress is negligible, and as *f(w)* is directly forced in the sensitivity analysis, the impact of the choice of stress function will not be discussed in this study.

The mathematical implementation of the *A*-r_s model is described in detail by Vilà et al. (2015).

2.6.3. Input for Modelling

This chapter describes what observations are used for both model initialization and evaluation. Figure 2.5 gives an overview of the data sets, and the specific values used for model initialization are given in Appendix B.

The particulars of the observations are organized according to the key model processes (which are described in detail in Chapter 9 in Vilà et al., 2015):

- **Soil**: The Clapp and Hornberger (Clapp and Hornberger, 1978) and other soil parameters, and volumetric moisture contents for wilting point, saturation, and field capacity are derived from the soil composition according to Ghildya et al., 1987[2]. For the top soil layer, soil moisture and temperature are taken from the data at 5 cm depth. For the lower layer the average soil moisture for the root zone (1-3 m depth) is taken from the value at 20 cm depth as it is close to field capacity. The skin layer conductivity is kept at default value.

- **Surface**: For surface temperature, specific humidity, and CO_2 concentration the profile measurements at the displacement height (2/3 canopy height; 30 cm) are used. Atmospheric pressure is taken from the EC system and is assumed constant over the first two meters of the surface layer. The *A*-r_s module is initialized with the default values

[2]Work by BSc. G. Miranda García for her master thesis, 2019

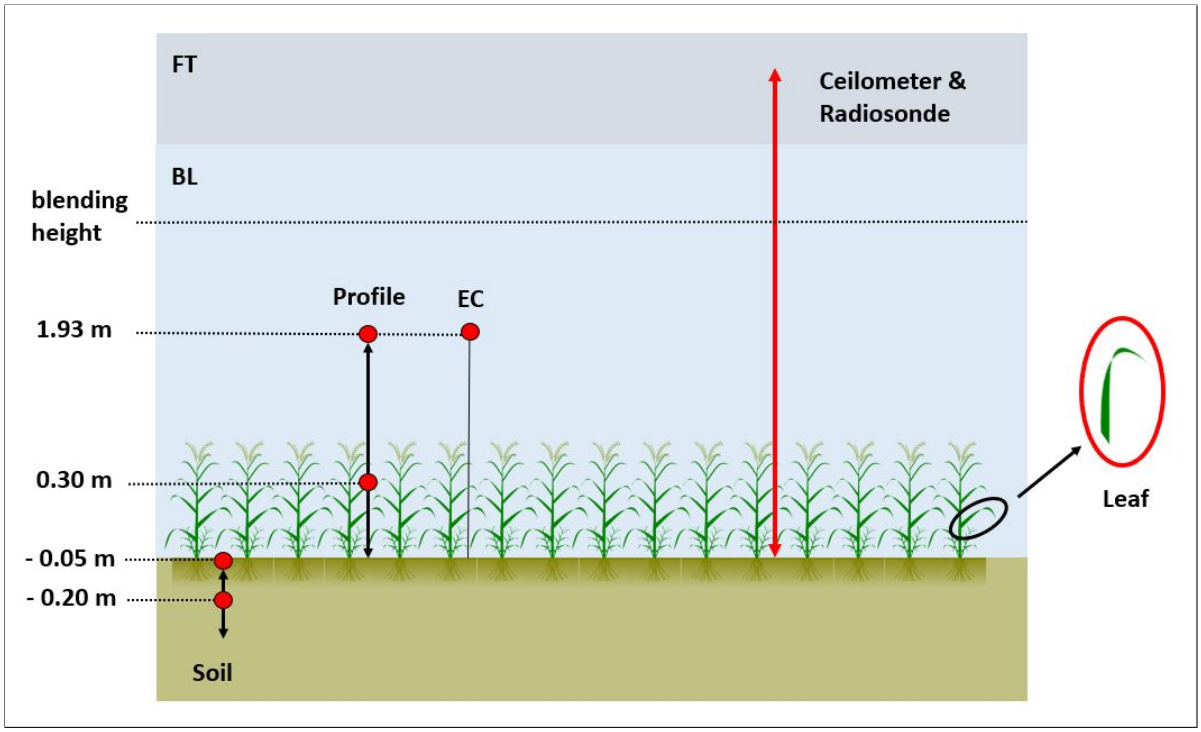

Figure 2.5: Schematic depiction of the measurements used for model initialization and evaluation. The used observations are marked in red, miscellaneous observations are black. Below the blending height the CloudRoots measurements are used to initialize and evaluate the model results, and above the blending height data from JOYCE and the radiosonde measurements.

for *C3*-plants. Mesophyll conductance at 298 K ($g_{m,298}$ [m s^{-1}]), CO_2 maximum primary production at 298 K ($A_{m,max,298}$ [mg m^{-2} s^{-1}]), and initial low light condition (α_0 [mg J^{-1}]) are derived from fitting the A-r_s model to the leaf level gas exchange data[3]. The roughness length for momentum (z_{0m} [m]) is taken as approximately 10% of canopy height minus the displacement height. The roughness length for scalars (z_{0h} [m]) is taken as $0.1 z_{0m}$ (Garratt and Hicks, 1973; Graf et al., 2014).

- **2 m values** for model evaluation: The values are taken from the profile measurements at 2 m.
- **ML values**: $\bar{\theta}$ is taken from the JOYCE and microwave and radiosonde data. As $\bar{q}$ and ML CO_2 data are lacking, the model is initialized in such a way that the derived 2 m values corresponds to the observations. In addition, the initialization value for $\bar{q}$ is cross-checked with the radiosonde data.
- **BL height**: From the radiosonde and JOYCE microwave and ceilometer data.
- **FT**: The jumps and lapse rates for q and θ are taken from the radiosonde data, by respectively approximating a discrete jump at BL height and fitting the first 1500 m above the jump to find the lapse rates.
- **Wind**: The surface friction velocity (u^* [m s^{-1}]) is taken from the EC measurements. As the quality of the ML and FT wind measurements is insufficient, the ML wind in zonal direction (u [m s^{-1}]), jump at BL height (Δu [m s^{-1}]), and FT lapse rate (γ_u [m s^{-1} m^{-1}]) are initialized in such a way that the modelled absolute wind speed matches the diurnal course measured with the sonic anemometer. Meridional wind values are set to zero.
- **Fluxes** for model evaluation: The values are taken from the EC measurements.

[3]Work by Dr. Hugo de Boer, Utrecht University

The requirement of strictly following the observations is relaxed for the initialization of $\bar{q}$. Until 8:00 the profile measurements show limited mixing above the canopy (i.e. non-uniform quantities), whereas the model requires well-mixed conditions. To bypass this incompatibility $\bar{q}$ is forced until 8:00 rather than initialized at 6:00 (Appendix B); with the restriction that the modelled evolution of the 2 m specific humidity agrees with the observations.

2.7. Sensitivity Analysis

To investigate the sensitivity of the ET-*VPD* hysteresis to the state of the surface and atmosphere, five sensitivity analyses will be performed. The impact on the shape of the ET-*VPD* hysteresis will be evaluated in terms of width, height, and steepness of the initial slope (Figure 2.6). As stomatal aperture is a key driving force of ET, also r_s is evaluated. In addition the conceptual model for ET derived in Chapter 1.2.2 (Equation 1.12) will be used to explain the results.

For the sensitivity study, the reference case is simplified to allow for better evaluation of the response of ET-*VPD* behaviour to the underlying processes. It is adapted by ignoring heat advection and intercepted water (morning dew). For each analysis one variable will be systematically varied:

1. **State of the surface**: Senescence determines the extent to which the vegetation can transpire. It can be caused by external and internal vegetation factors. Therefore the impact of senescence on ET-*VPD* hysteresis is investigated in two ways:

    - The soil moisture availability function *f(w)* (Equation 2.18) will be varied between 0 (where plants are fully stressed as there is no soil moisture available for evaporation) and 1 [-] (where the vegetation experiences no stress as there is unlimited soil moisture available).
    - The maximum capacity to assimilate CO_2 for photosynthesis will be varied via its maximum assimilation rate at 298 K ($A_{m,max,298}$ [mg m^{-2} s^{-1}]; for a detailed description see Appendix E in Vilà et al., 2015) as it is an internal plant property rather than a soil condition. $A_{m,max,298}$ will be varied between 1.98 (observed maximum for vegetation in full growth under no stress) and 0.04 mg m^{-2} s^{-1} (vegetation in near full senescence).

    Soil moisture stress may be a transient effect where after the vegetation may recover, whereas photosynthetic capacity will never increase again once it has been reduced due to senescence. Evaluating their impacts separately allows for separation of plant internal and external effects.

2. **State of the atmosphere**: Entrainment of warm, dry air will be varied by varying the strength of the inversion layer between the BL and RL. The inversion strength is defined in terms of $\Delta\theta_v$, and is set by the magnitudes of the jumps in potential temperature ($\Delta\theta$) and specific humidity (Δq). Many different combinations of the variables exist, but in view of time this study limits itself to a combined variation: $\Delta\theta$ and Δq respectively vary between 1 and 4 K, and between 0 and -5.10^{-3} kg kg^{-1}. Therefore, with an initial $\bar{\theta}$ of 286.2 K and $\bar{q}$ of 6.9.10^{-3} kg kg^{-1}, the corresponding initialized inversion strength in terms of the virtual potential temperature jump ($\Delta\theta_v$) ranges from 1.0 to 3.1 K.[4]

3. **Synoptic forcing**: Subsidence in terms of large-scale divergence (*div(U)*) will be applied to investigate the effect of a nearby high pressure region. *div(U)* will be varied from 0 to 10^{-5} [s^{-1}], leading to a subsidence velocity of 0 to -0.01 m s^{-1}.

[4] Ideally variations in $\Delta\theta$ and Δq are studied independently. Both quantities impact $\Delta\theta_v$ in a different way (Equation 1.10 in combination with 1.9), and therefore also w_e (Equation 2.3) and the ensuing BL growth (Equation 2.1). Furthermore, variations in $\Delta\theta$ and Δq have their respective impacts on the linked ML quantities $\bar{\theta}$ and $\bar{q}$ (Equations 2.5 and 2.7). The combined impact of these processes leads to changes in L_vE and *VPD*. By varying $\Delta\theta$ and Δq at the same time, it becomes impossible to untangle the respective impacts of these processes. Therefore, in hindsight the choice to co-vary $\Delta\theta$ and Δq should have been avoided.

4. **Turbulent mixing**: r_a is increased to investigate the impact of reduced mixing between the surface and ML values for specific humidity, temperature, and CO_2. This reflects for example lower wind speeds or increased canopy height. The modelled diurnal course for r_a can only be forced by increasing its value with a constant increment at every model iteration, and not as an initialization condition: At every time step r_a is increased by adding between 0 and 50 [s m^{-1}] to its modelled value.

The imposed parameter ranges are summarized in Table 2.2.

Variable	1	2	3	4	5	6	7	8	9	10
f(w) [-]	1.0	0.9	0.8	0.7	0.6	0.4	0.3	0.2	0.1	0.0
$A_{m,max,298}$ [mg m^{-2} s^{-1}]	1.98	1.77	1.55	1.33	1.12	0.90	0.69	0.47	0.26	0.04
div(U) [10^{-6} s^{-1}]	0.0	1.1	2.2	3.3	4.4	5.6	6.7	7.8	8.9	10
Δr_a [s m^{-1}]	0.00	5.56	11.1	16.7	22.2	27.8	33.3	38.9	44.4	50.0
$\Delta\theta$ [K]	1.0	1.3	1.7	2.0	2.3	2.7	3.0	3.3	3.7	4.0
Δq [10^{-3} kg kg^{-1}]	0.0	-0.6	-1.1	-1.7	-2.2	-2.8	-3.3	-3.9	-4.4	-5.0
$\Delta\theta_v$ [K]	1.0	1.2	1.5	1.7	2.0	2.2	2.4	2.7	2.9	3.1

Table 2.2: Imposed parameter ranges for the sensitivity analysis. The *Variable* column lists the imposed initial conditions. The last row lists the initialization values for $\Delta\theta$ and Δq for each step of the entrainment forcing, with in addition the corresponding $\Delta\theta_v$ value. The numbers 1-10 also represent the position on the horizontal axis of Figure 4.1, from left to right.

In 2004 Zeppel et al. proposed to quantify hysteresis as the area bound by the ET-*VPD* loop, and to normalize by dividing ET (in terms of sap flow or tree water use) by its diurnal maximum. Zhang et al. (2014) adopt this approach, and also normalize *VPD* by setting the diurnal minimum to zero and maximum to 1. Although normalization and quantifying the area allows for some sort of comparison between studies, it has no theoretical foundation and important information on atmospheric and surface conditions may be lost. Therefore this study uses straightforward metrics from non-normalized curves as shown in Figure 2.6:

- **Width**: The difference between the diurnal maximum and minimum of the *VPD* [Pa];
- **Height**: The diurnal maximum of L_vE [W m^{-2}];
- **Initial slope**: The ET-*VPD* slope between 6:00 and 10:00 [W m^{-2} Pa^{-1}];
- **Afternoon r_s**: The average r_s from 11:00 to 15:00 [s m^{-1}].

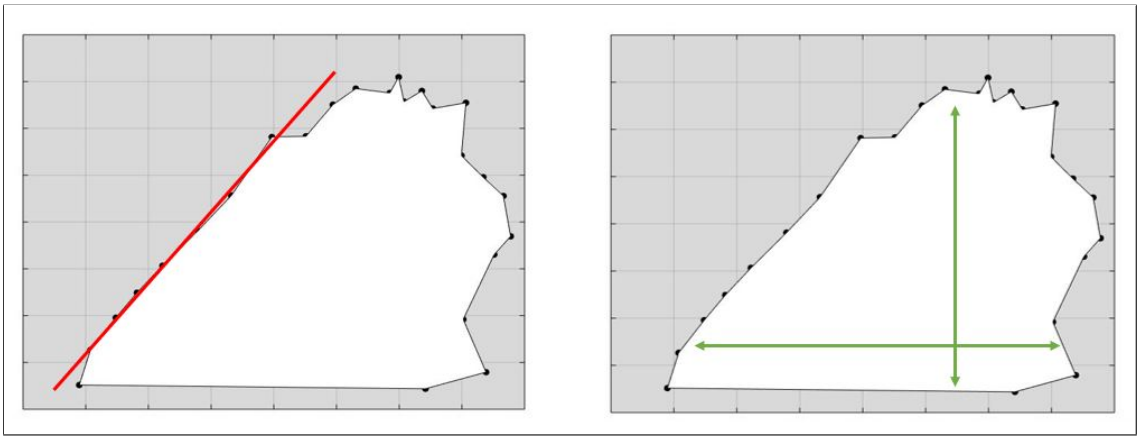

Figure 2.6: Metrics for hysteresis shape analysis, shown for a typical ET-*VPD* hysteresis curve with *VPD* [a.u.] on the horizontal axis and L_vE [a.u.]. on the vertical axis. Red: Initial slope; Green: Maximum L_vE (height) and diurnal variation in *VPD* (width).

With this approach and by analysing ET-*VPD* hysteresis shape for various surface, BL, and synoptic conditions this study extends previous work and aims to lay a new foundation for ET-*VPD* hysteresis research. The results of the sensitivity analysis will be further described in the Chapter 3.1.

3

Results

In this chapter the results are presented. Chapter 3.1 describes ET-*VPD* hysteresis loops observed in the CloudRoots campaign during spring and summer 2018. Next, the results for modelling the reference case are shown in Chapter 3.2. The ensuing sensitivity analysis (Chapter 3.3) demonstrates the effects changes in surface conditions and BL dynamics have on ET-*VPD* hysteresis by means of five cases. These results are discussed in terms of underlying processes.

3.1. Observations

To assess the overall behaviour of diurnal ET-*VPD* hysteresis loops and discern potential drivers, the selected loops are shown in Figure 3.1.

Five loop types are identified, indicated by the different colors in Figure 3.1:

- **Full photosynthesis (green)**: Maximum ET approaches the diurnal maximum for available energy ($Q^* - G$). The composite effect of a more moist atmosphere with reduced surface and BL warming due to the reduced H, leads to a relatively modest diurnal maximum of *VPD*. These loops all occur when the vegetation is green, in full growth, and under no stress: The stomata are fully open to maximize CO_2 uptake.
- **Slight reduction of photosynthesis (blue)**: Transition phase between green and purple loops. Maximum ET is somewhat reduced whereas maximum *VPD* has increased. Chronologically these loops lies between the green and purple loops. The vegetation has reached maximum crop height and some senescence is visible by browning of the leaves; either due to lack of soil moisture or by other stressors.
- **Significant reduction of photosynthesis (purple)**: Maximum ET reaches about 40% of the diurnal maximum for available energy. Reduced ET leads to a dryer and warmer atmosphere, and thus a high maximum *VPD*. These loops occur late in the growth season when the vegetation is in senescence (visible by the yellow-brown colour).
- **No photosynthesis (red)**: Very low maximum for ET, with any remaining ET resulting from soil evaporation. The curve has relatively modest *VPD*, most likely due to coincidence. This curve occurs late in the season when the vegetation is in full senescence.
- **Miscellaneous (black)**: Loops are truncated both in maximum ET and *VPD*. These loops occur over the entire growth season. This regime appears to be primarily correlated with green vegetation and significantly reduced morning *PAR* due to clouds. However, the number of loops is too small to draw a definite conclusion on their origin.

The diurnal hysteresis curves in Figure 1.1a show a clear imprint of senescence on loop shape, and in particular the initial slope - where senescence is strongly correlated to stomatal aperture as it reflects the vegetation's ability to excrete water. However, within each parameter regime there still are significant differences in the diurnal ET-*VPD* signatures, especially in the relative *VPD* width with respect to maximum ET. Solely looking at one specific surface or BL variable, such as wind speed or early morning temperature, can only partly explain the differences between the curves. Therefore, BL dynamics such as entrainment are suspected to cause these loop deformations.

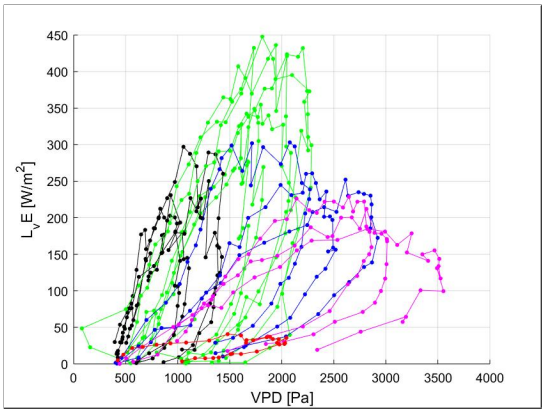

Figure 3.1: Repetition of Figure 1.1a: Diurnal hysteresis between ET and atmospheric moisture demand, measured with EC. ET is quantified as latent heat flux (L_vE [W m^{-2}]), and atmospheric demand as vapor pressure deficit (*VPD* [Pa]). (a) Composite of multiple diurnal loops where different colours indicate similar parameter regimes; Green: May 7-8-12-21-26 and June 6; Blue: June 10-28-29; Purple: July 1-2-3; Red: July 9; Black: May 11-18-19 and June 9 2018.

Observations alone are unable to explain all variations. Therefore a model is needed that incorporates the essential underlying dynamics to systematically analyse the impact of surface and BL processes on the ET-*VPD* hysteresis characteristics. The observed ET-*VPD* signatures give the metrics to assess the shape of hysteresis loops in the sensitivity analysis: Initial slope, maximum diurnal ET, and maximum diurnal change in *VPD* (Chapter 2.7). As the canopy resistance is the key driver for ET, its diurnal course (Chapters 3.2 and 3.3) and afternoon (11:00-15:00) average (Chapter 4) are also used for interpretation of the result.

3.2. Modelling: Proof-of-Concept

The second aim of the thesis is to deliver a proof-of-concept for prognostically modelling ET-*VPD* hysteresis with a ML model that couples atmosphere and surface and incorporates vegetation mechanistics. To do so, the model is initialized with the 6:00 conditions for 7 May 2018 (Appendix B). The resulting diurnal courses of the output variables are assessed against the measured quantities. Below, the observations and model results are shown for the key quantities: Q^*, BL height, $\tilde{\theta}$, L_vE, H, and 2 m θ, 2 m q, 2 m *VPD*, 2 m U, as well as the resulting ET-*VPD* hysteresis loop. In addition the modelled aerodynamic and stomatal resistances are assessed. The model results are cut off at 16:30, as shortly after this time a stable BL starts to form from below and the model assumption of well-mixed conditions no longer holds (Figure 3.3).

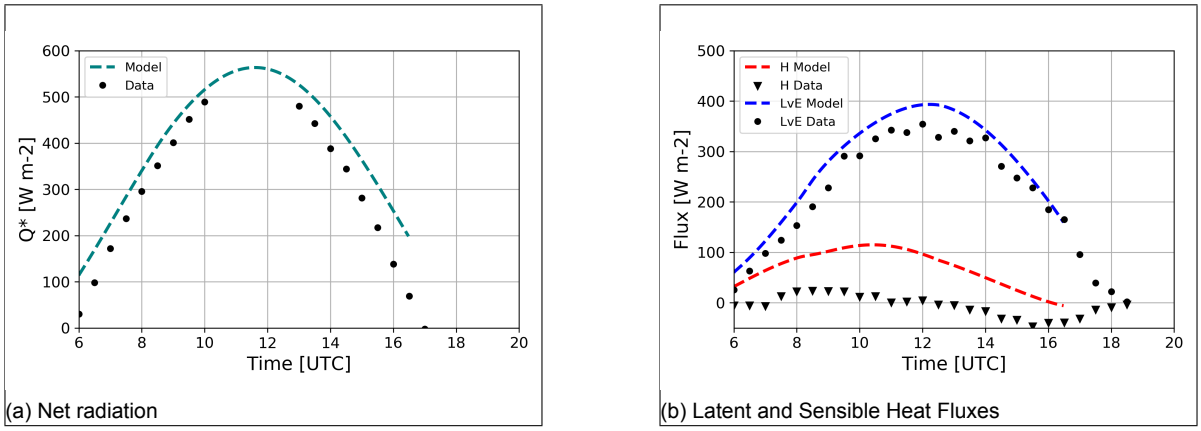

Figure 3.2: Modelled and observed radiant and turbulent surface fluxes: (a) Net radiation (Q^*), and (b) sensible (H) and latent heat fluxes (L_vE). Modelled quantities are indicated by the dashed line, observations by individual points.

Figure 3.2 shows both the main driving force of the system's diurnal evolution, Q^*, and the resulting heat fluxes H and L_vE. Q^* follows the tendency of the observations, with a slight overestimation due to assumptions on the absence of aerosols (impacting S_{in}; Barbaro et al., 2014), the surface and atmosphere emissivities (impacting L_{in} and L_{out}), the albedo (taken as a fixed value rather than an evolving quantity, impacting S_{out}), and deviations in modelled θ_s and θ_a (impacting L_{in} and L_{out}). L_vE is reproduced by the model at a higher value with respect to the observations. This aspect could be due to model limitations, as well as to limitations in the observational method itself: Wang et al. (2012) and Malek (1993) discuss how the EC systematically underestimates L_vE. The maximum modelled H is much higher than the values measured at the site and reaches over 100 W m^{-2}. The H observed at the field is suppressed by the advection of warm air (Chapter 2.4). The modelled H is more representative for the area as a whole: As described in Chapter 2.4, this landscape flux is set by an aggregate of surfaces that generally have a much larger H than the well-watered study site. The turbulent surface fluxes are thus well reproduced by the model, with L_vE reflecting the field-scale ET and H its landscape-scale aggregate that is required to grow a representative BL.

Together, H and L_vE result in the surface kinematic buoyancy flux $(\overline{w'\theta_v'})_s$ (Equation 2.4) that drives atmospheric stability and BL growth. The flux can be converted to the virtual heat flux in W m^{-2} by multiplying with ρc_p; the observed and modelled courses are shown in Figure 3.3. Observations show that after 14:00 the flux becomes negative, which appears to indicate that the layer adjacent to the surface becomes stable. However, the magnitude of the flux is -25 W m^{-2} at its minimum at 16:00, which lies within the uncertainty of the measurements. Furthermore, at 14:00 L_vE is 300 W m^{-2} (Figure 3.2), which is only possible in case of a sufficient atmospheric moisture deficit (Equations 2.14-2.16), which requires well-mixed conditions (for the circumstances of the reference case). Therefore we conclude that also after 14:00 the BL is unstable. This is confirmed by Mahrt (1999) who describes that as long as there is sufficient wind and the surface heterogeneity is local (smaller than 10-100 km; as is the case for the study site), generally no internal boundary layers develop. The virtual heat flux also is zero before 7:00; however, due to the low values of H and L_vE no conclusion can be drawn about the stability of the lowest part of the BL. The modelled virtual heat flux becomes positive before 6:00, ensuring that the sensitivity analysis is based on a well-mixed case. In the evening, the modelled virtual heat flux becomes negative at 16:52.

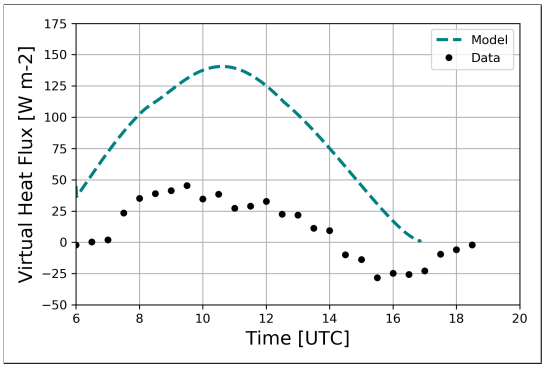

Figure 3.3: Modelled and observed surface virtual heat flux $\rho c_p \overline{w'\theta_v'}$. The modelled flux becomes negative at 16:52.

The turbulent heat fluxes combined with the imposed heat advection drive the diurnal evolution of the BL, with the BL height as the large-scale resultant of entrainment (Equation 2.1), as shown in Figure 3.4a. The modelled BL height values correspond to those measured with microwave (black triangles) and lidar (red stars). The model reproduces the onset and ending of rapid BL growth as well as the maximum BL height. The 12:00 radiosonde observation (blue) is taken at a location 100 km from the site and shows a BL height comparable to the microwave and lidar measurements, demonstrating the uniformity in BL height over large distances and justifying the assumption on landscape-driven BL growth. Figure 3.4b shows $\bar{\theta}$: The model reproduces its diurnal evolution closely, both for the microwave and radiosonde measurements. The minor slope change around 9:00 is caused by the rapid increase of heat advection (Appendix B.2). ML CO_2 concentration and $\bar{q}$ are not shown as there are no observations to validate the model against.

As ET and *VPD* are both observed at 2 m, the 2 m model quantities for θ and q are crucial in providing the proof-of-concept, and are shown in Figure 3.5. The 2 m θ and q are determined

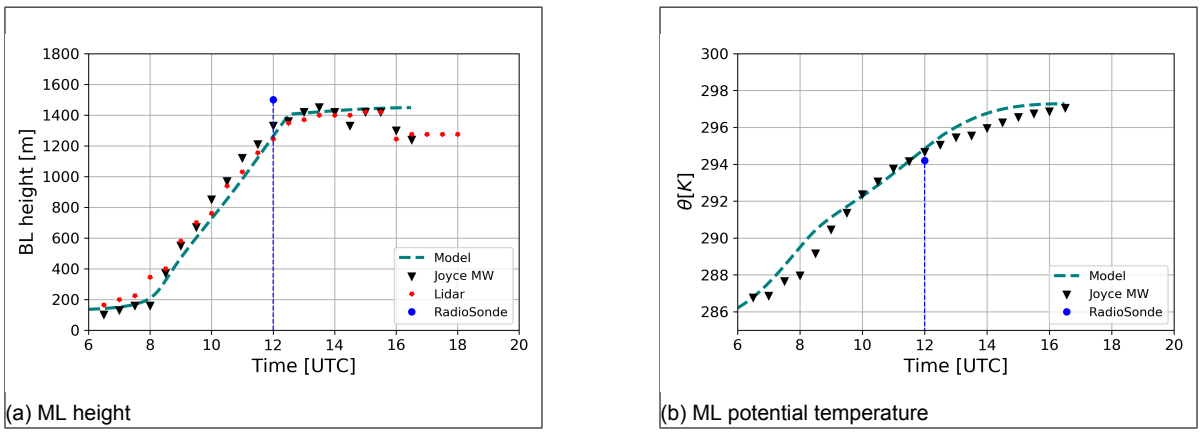

Figure 3.4: Modelled and observed ML values: (a) ML height (h), and (b) potential temperature ($\bar{\theta}$). Modelled quantities are indicated by the dashed line, observations by individual points. MW stands for microwave measurements.

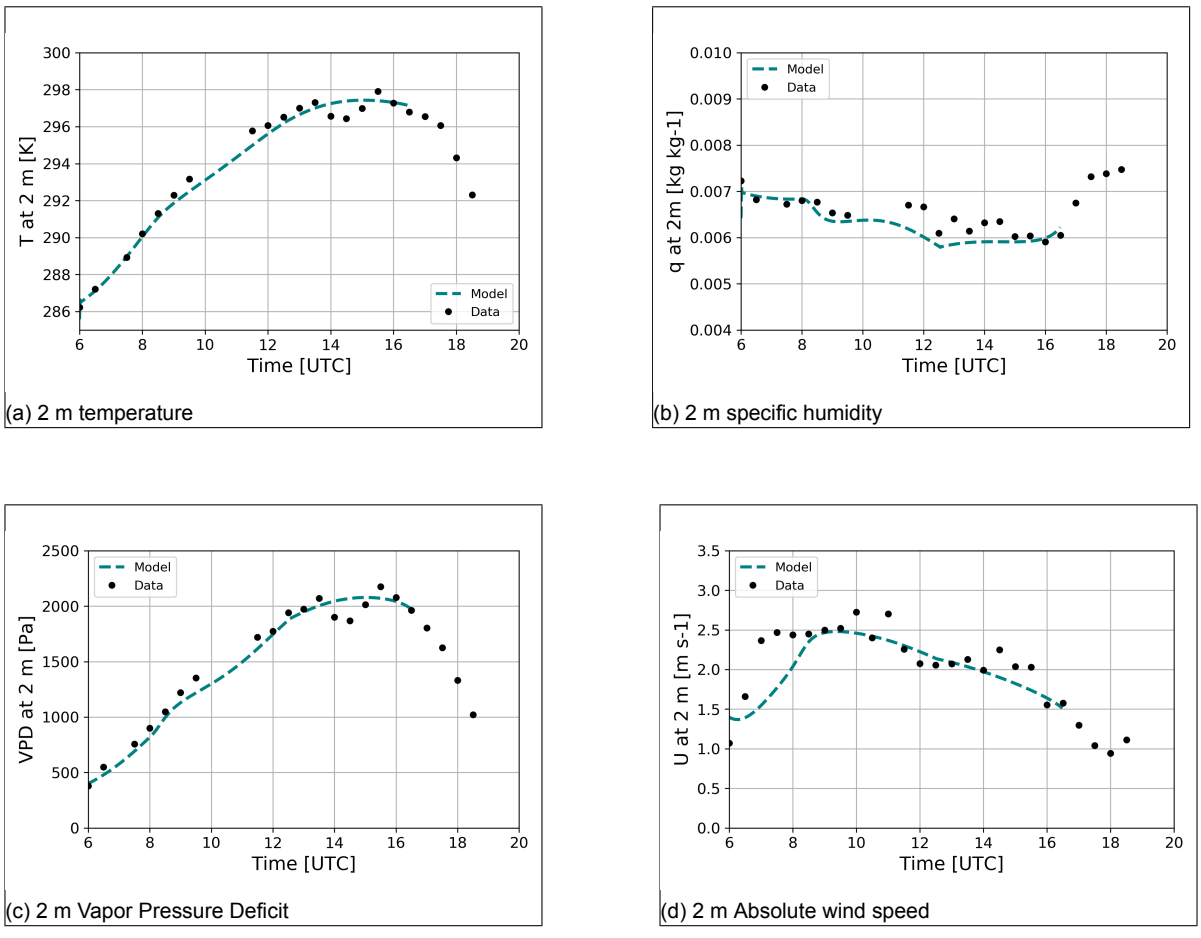

Figure 3.5: Modelled and observed 2 m quantities: (a) Temperature; (b) Specific humidity; (c) Vapor Pressure Deficit; And (d) absolute wind speed. Modelled quantities are indicated by the dashed line, observations by individual points.

by their respective surface and ML values and the SL interpolation. Both the tendency and magnitude of the 2 m θ and q agree well with the measurements. The characteristic 14:00 depression in 2 m θ (Figure 3.5a) that is observed by both the profile measurements and EC, may be caused by an additional advection event and is not accounted for in the present study. The magnitude of the 2 m q (Figure 3.5b) also agrees well. The observations show a pronounced increase in 2 m q from 16:00 to 18:00. The model is able to reproduce the

onset of this rapid increase in q, as a negative modelled $\overline{(w'\theta_v')}_s$ leads to a stable atmosphere. This indicates that atmospheric stability and the aerodynamic resistance (Equation 2.17) are accounted for. As the modelled and observed 2 m θ and q agree well, the same holds for the *VPD* at 2 m (Equation 1.1; Figure 3.5c). The modelled curve shows that the impact of $\bar{q}$ being forced until 8:00 is negligible: The 2 m *VPD* behaviour is dominated by temperature until well after 12:00 as the BL keeps growing (Figure 3.4a). Last, the absolute wind speed U at 2 m is shown (Figure 3.5d) as the wind - together with atmospheric stability - sets the aerodynamic resistance (Equation 2.17). The modelled 2 m U agrees well with the overall tendency of the observations, except before 8:00 where 2 m U is underestimated. The underestimation of 2 m U in turn has an impact on the 2 m q, motivating the choice to force $\bar{q}$ until 8:00.

As there are no vegetation skin measurements available for temperature and specific humidity, the diurnal courses for modelled θ_s and q_s are difficult to validate. Below we will motivate that it is not straightforward to compare modelled values with the measurements. The model assumes an infinitely shallow surface, defined as the location where the impact of the wind is no longer felt. This generally corresponds to the observational displacement height at 2/3 of the canopy (here: 0.30 m), as described by Moene and Van Dam (2014). θ_s and q_s are determined from the in-canopy profile measurements at 30 cm height. However, these are atmospheric rather than leaf surface values. In reality, θ_s is higher than its atmospheric equivalent (Panwar et al., 2019) due to local heating of the leaves and minimal in-canopy mixing by wind. Similarly, q_s is higher close to the stomata (Jarvis and McNaughton, 1986) than in the surrounding atmosphere. Due to this discrepancy between the physical situation and model setup, both the actual and modelled θ_s and q_s are higher than the respective observed atmospheric quantities at 0.30 m (not shown as quantitative comparison is impossible).

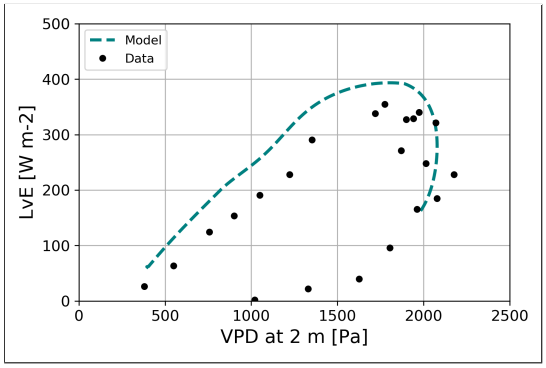

Figure 3.6: Modelled and observed ET-*VPD* hysteresis. Modelled quantities are indicated by the dashed line, observations by individual points. The model was switched off at 16:30 as shortly after this time the well-mixed condition is broken, thus resulting in an unclosed hysteresis loop.

The resulting ET-*VPD* hysteresis loop is shown in Figure 3.6. The modelled curve follows the observations well. The minor discrepancy between observations and modelling is primarily caused by the overestimation of ET (Figure 3.2); However, the difference lies within measurement and model uncertainties. The figure therefore gives the proof-of-concept for modelling ET-*VPD* hysteresis with a ML model that incorporates the biological responses of the vegetation, and couples surface and atmosphere.

Apart from setting up and validating the reference case, the model also allows evaluation of r_a and r_s. Figure 3.7 shows that during the entire day r_a is higher than r_s, which is typical for low vegetation under well-watered conditions (Moene and Van Dam, 2014). However, contrary to the often used assumption, both resistances are not constant in time and undergo a distinct semi-parabolic course. The diurnal course for r_a is inversely proportional to both the wind speed and a drag coefficient C_s (Equation 2.17). C_s non-linearly depends on the height of the surface layer (10% of the BL height), the Obukhov length L [m] (that in turn depends on $\overline{(w'\theta_v')}_s$), and the roughness lengths for momentum z_{0m} [m] and heat z_{0h} [m]. The high morning values for r_a are primarily caused by the wind speed, whereas the sharp increase of r_a around 16:00 is caused by a strong decrease in $\overline{(w'\theta_v')}_s$. The tendency of r_s is driven by *PAR* as the reference case is at near-optimal conditions in terms of temperature, *VPD*, and soil moisture. These results show the limitation of the conceptual model for ET: Although it can explain the overall ET-*VPD* tendency in terms of the order of magnitude of the respective resistances, it oversimplifies the diurnal pattern for r_a and r_s.

In summary, by imposing heat advection H is representative of the aggregate of the landscape scale fluxes (see Figure 2.2a), whereas L_vE reflects the field-scale ET. With this interpretation we are able to model the relevant physical quantities, from the driving force of daytime BL evolution, Q^*, to BL height. The diurnal evolution of all variables of interest was reproduced. In view of the model's capability the resulting modelled ET-*VPD* hysteresis loop corresponds very well with the observations. Thus the proof-of-concept is delivered for the proposed modelling approach.

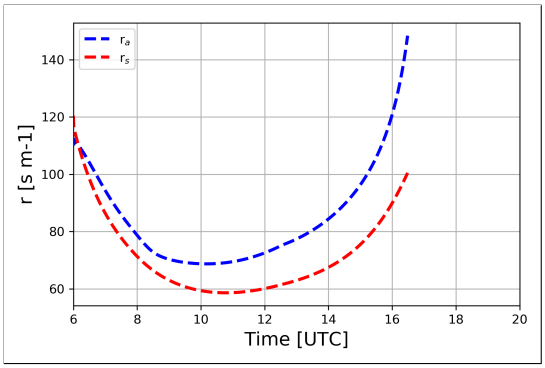

Figure 3.7: Modelled diurnal courses for r_a and r_s.

3.3. Modelling: Sensitivity Analysis

For the sensitivity analysis the reference case is simplified by ignoring morning dew (Appendix B.1) and the advection required to incorporate the landscape scale sensible heat flux (Chapter 2.4 and Appendix B.2). These effects are not essential in studying ET-*VPD* hysteresis and unnecessarily complicate the interpretation of the sensitivity study. All other initialization conditions are identical to that of the reference case. With the adapted reference case, the impact of altered conditions on ET-*VPD* hysteresis shape is evaluated: Respectively the input for soil moisture availability, CO_2 assimilation capacity, large-scale horizontal wind divergence, strength of the inversion layer, and the aerodynamic resistance are systematically varied (Chapter 2.7). The results are evaluated in terms of the initial slope of the ET-*VPD* curve, maximum ET, maximum diurnal *VPD* change, and stomatal behaviour (Chapter 2.7).

3.3.1. Surface State: Soil Moisture

Figure 3.8 shows the impact of soil moisture availability, where the reference case corresponds to *f(w)* = 0.9. As soil moisture stress increases - and *f(w)* decreases - ET progressively decreases (Figure 3.8a), leading to reduced surface and atmospheric q. Changes in available energy (Q^* - G) are small with respect to the change in ET. A decreased ET therefore leads to an increased H via the surface energy partitioning (Equation 2.13), and consequently to strongly elevated surface and atmospheric temperatures (respectively over 4 and 10 K at the diurnal maximum). This process is described by Equation 2.5 where an increase in H leads to an enhanced tendency for $\bar{\theta}$. And, as both H and $\bar{\theta}$ are higher, calculating θ_s from the surface energy balance shows that it must also increase. Due to the combined impact of a - non-linearly, due to the Clausius-Clapeyron relation for saturation pressure - increasing 2 m θ and decreasing 2 m q, 2 m *VPD* strongly increases at all heights in the ML. Therefore, increasing soil moisture stress - i.e. decreasing *f(w)* - results in a significant increase of diurnal 2 m *VPD* width and decrease of the early morning slope of the hysteresis loop.

Figure 3.8b shows the non-linear response of vegetation to changing soil moisture availability. The different scale of the vertical axis (with respect to Figure 3.7) hides the impact of the diurnal *PAR* cycle. For low soil moisture stress (*f(w)* = 1 to 0.7) r_s is only slightly offset by the changing conditions. As *f(w)* further decreases r_s rises rapidly. When *f(w)* drops below 0.3 a transient mid-afternoon elevation of r_s appears, whose impact can be seen in the resulting ET depression in the ET-*VPD* curves. For the case of *f(w)* = 0 there still is a residual L_vE of approximately 100 W m^{-2} due to soil evaporation. This residual results from the vegetation *f(w)* function not impacting the modelled soil evaporation. In addition, the vegetation transpiration model incorporates a minimum cuticular conductance that is independent of *f(w)*: An assumption that is violated under extreme soil moisture stress.

However complex the underlying processes, the conceptual model of ET (Equation 1.12) can help explain the change in initial ET-*VPD* slope. As discussed in Chapter 1 and shown in Figure 3.8b, vegetation that experiences soil moisture stress will reduce the aperture of

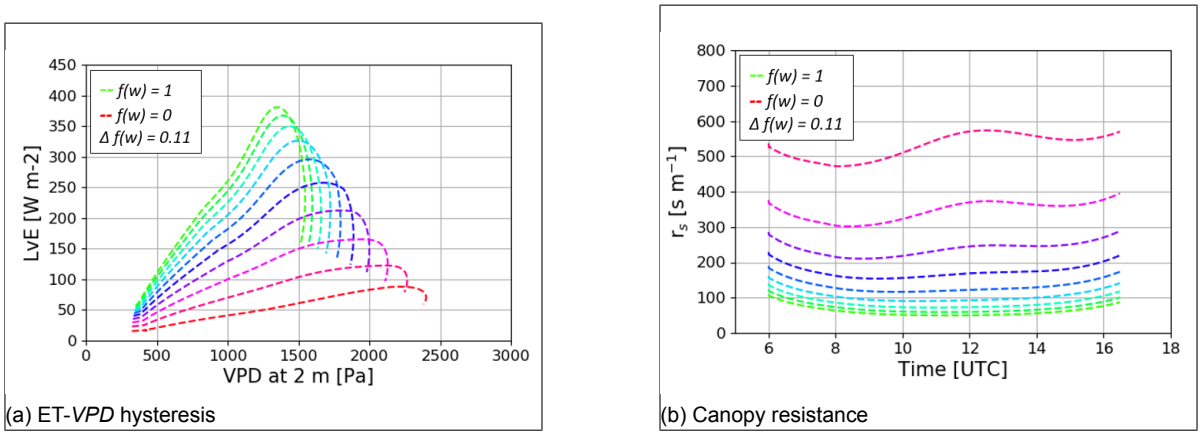

Figure 3.8: Sensitivity analysis: Variation in soil moisture availability function *f(w)*. From green to red the curves represent the cases from no stress (*f(w)* = 1 [-]) to fully stressed conditions (*f(w)* = 0 [-]) (a) ET-*VPD* hysteresis; (b) r_s.

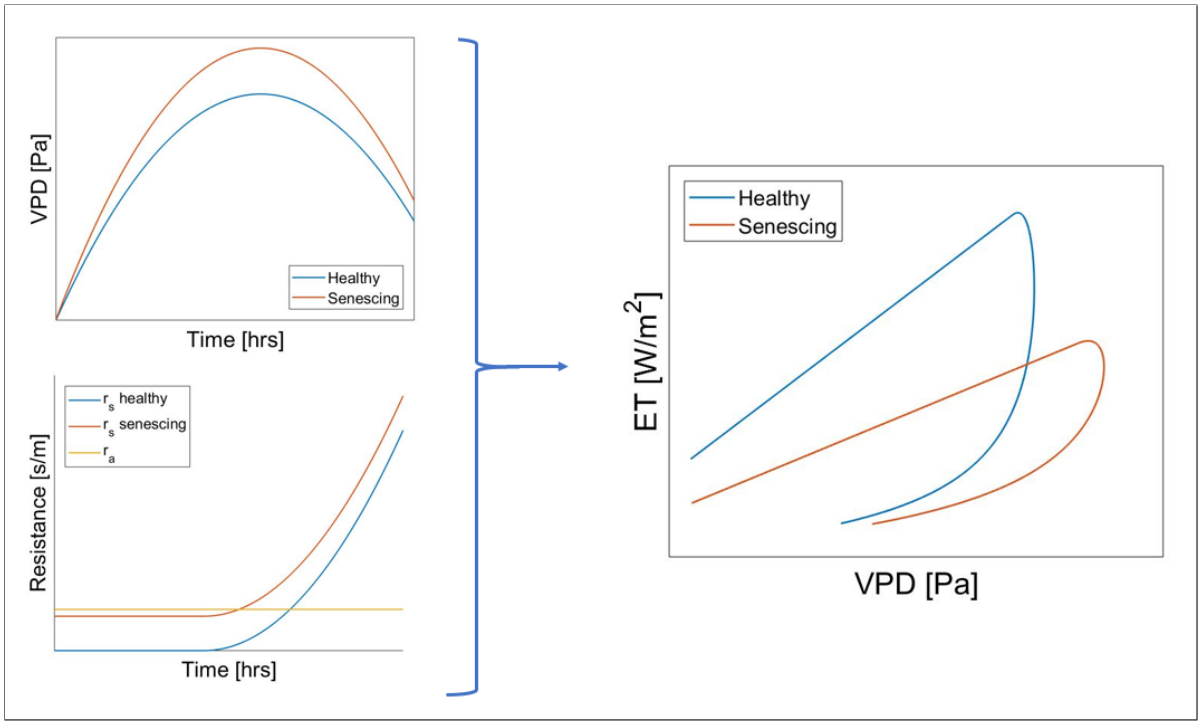

Figure 3.9: Conceptual model for ET simulating the impact of senescence. Upper left: *VPD* where senescence is set by soil moisture stress; the subscript *healthy* refers to vegetation in full photosynthesis at no soil moisture stress, and *senescing* to vegetation feeling the impact of reduced soil moisture. Lower left: Idealized diurnal course for aerodynamic (r_a) and canopy resistances (r_s). Right: The resulting ET-*VPD* curves.

its stomata throughout the day. As a result the canopy resistance will increase, causing ET to reduce. Due to the reduced ET, H increases (Equation 2.13). As H is the dominant term in $\overline{w'\theta_v'}$ (Equation 2.4), $\overline{w'\theta_v'}$ also increases. This leads to more entrainment of relatively warm dry air (Equation 2.3) and hence an increase in *VPD*, via temperature changes (Equation 2.5) dominating those of specific humidity changes (Equation 2.7). A conceptual picture of the resulting resistances and *VPD* is given in the left hand of Figure 3.9. In case of senescence, r_s is given an offset with respect to healthy vegetation; and the diurnal variation of r_a and r_s is neglected as they are small with respect to soil moisture induced changes in r_s. Although the offset of r_s is minor with respect to the magnitude of r_a, the impact is clearly visible in the resulting ET-*VPD* curve: The combined increase in r_a and r_s causes a significant reduction in ET for similar *VPD*. At the same time, the diurnal maximum for *VPD* is higher when the

vegetation is able to transpire less. Thus causing the initial slope to be lowered, as observed in Figure 3.8a.

3.3.2. Surface State: Photosynthetic Capacity

The impact of the vegetation's internal capacity to assimilate CO_2 for photosynthesis is shown in Figure 3.10. The reference case corresponds with the measured maximum rate at which the vegetation can assimilate CO_2 ($A_{m,max,298}$ = 1.98 mg m^{-2} s^{-1}). The hysteresis curves (Figure 3.10a) show threshold behaviour: For values as low as $A_{m,max,298}$ = 0.47 mg m^{-2} s^{-1}, decreasing photosynthetic capacity barely has any impact. As $A_{m,max,298}$ drops further, the curves exhibit a similar tendency as for decreasing soil moisture availability: ET decreases progressively, combined with a concurrent increase in *VPD*. The underlying BL dynamics are equivalent to those described in Section 3.3.1. For the minimum value of $A_{m,max,298}$ there still is residual ET, both due to the remaining capacity to assimilate CO_2 (modelling $A_{m,max,298}$ = 0 mg m^{-2} s^{-1} in inhibited due to asymptotic behaviour of the vegetation transpiration model) and to soil evaporation.

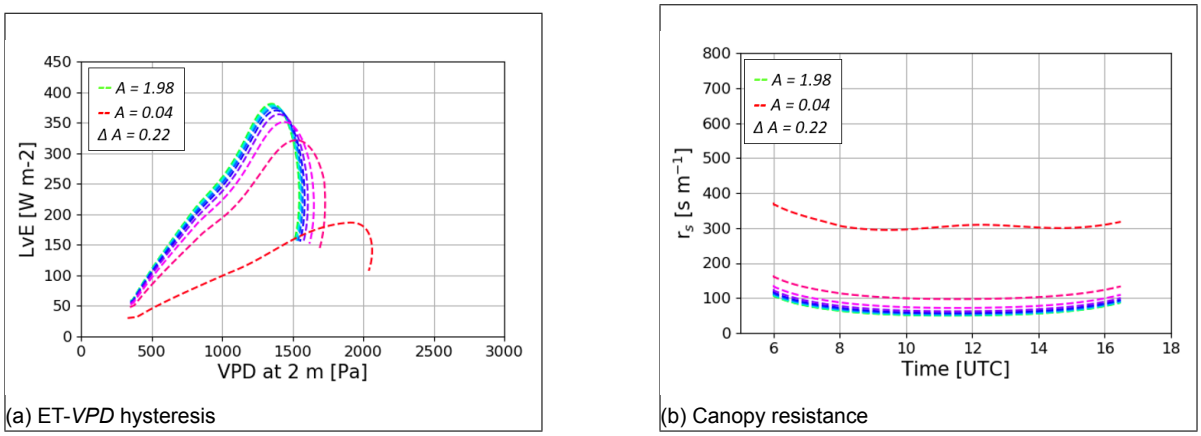

Figure 3.10: Sensitivity analysis: Variation in maximum capacity of plants to assimilate CO_2 for photosynthesis ($A_{m,max,298}$) at 298 K. From green to red the curves represent the cases from no ($A_{m,max,298}$ = 1.98 mg m^{-2} s^{-1}) to high senescence ($A_{m,max,298}$ = 0.04 mg m^{-2} s^{-1}). (a) ET-*VPD* hysteresis; (b) r_s. In the legend, *A* denotes $A_{m,max,298}$.

The tendency of r_S (Figure 3.10b) confirms the hysteresis behaviour, with r_S only rising significantly for the lowest values of $A_{m,max,298}$. As for the case of extreme soil moisture stress, the r_S curve for $A_{m,max,298}$ = 0.04 mg m^{-2} s^{-1} shows a slight mid-afternoon depression of ET.

Figure 3.10 shows a remarkable consequence of a decrease in capacity to assimilate CO_2: As ET is not limited by soil moisture, the plants keep their stomata open and transpire, irrespective of CO_2 uptake. Only when senescence is advanced to an extent that water paths or stomatal tissue dry out, transpiration is reduced.

3.3.3. Boundary Layer State: Subsidence

Most literature on *VPD* hysteresis has only focused on the effect of surface changes on ET-*VPD* hysteresis. However, synoptic forcing may also have an impact on hysteresis characteristics. In this chapter the impact of large-scale subsidence is studied. This is done in terms of large-scale wind divergence (*div(U)*), where subsidence advection is neglected. *Div(U)* is varied between 0 (no subsidence; as for the reference case) and 1.10^{-5} s^{-1}. The results are shown in Figure 3.11.

Equation 2.1 shows how under subsidence, BL growth is controlled by both entrainment (represented by w_e; Equation 2.3) and synoptic effects (represented by w_s; where *div(U)* is imposed and h is calculated by the model). Positive divergence is equivalent to negative w_s (Equation 2.2), and the imposed subsidence suppresses BL growth (Equation 2.1). At maximum divergence the BL height grows to approximately 1100 m, leading to a vertical

subsidence velocity w_s of -0.01 m s^{-1} (Equation 2.2) at the top of the BL. As the relative change in BL height is small, the imposed subsidence only leads to a modest increase in $\bar{\theta}$ (Equation 2.5) and $\bar{q}$ (Equation 2.7) - where these changes are small enough not to significantly impact either L_vE or H. Surface θ, q, and *VPD* remain virtually unchanged under the imposed subsidence. Hence, the vegetation resistance r_s (not shown) is not affected by large-scale subsidence.

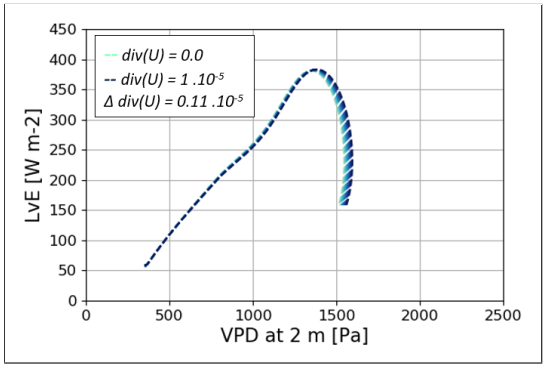

Figure 3.11: Sensitivity analysis: Impact of variation in subsidence due to large-scale divergence on ET-*VPD* hysteresis. From light to dark blue the curves represent the cases from no (*div(U)* = 0 s^{-1}) to high subsidence (*div(U)* = 1.10^{-5} s^{-1}).

The 2 m θ and q lie between their respective surface and ML values (calculated with the SL gradient), and are less affected than $\bar{\theta}$ and $\bar{q}$. Therefore, the 2 m *VPD* only varies to a minor extent depending on the degree of subsidence. However small, the effect of subsidence on 2 m *VPD* peaks as h reaches its late afternoon maximum, thus explaining why the ET-*VPD* curves only change for the late afternoon. Maximum L_vE and initial slope remain the same.

Furthermore, as ET is plotted against 2 m *VPD* rather than the - unaffected - surface *VPD*, the modelled changes in hysteretic behaviour can uniquely be attributed to the evaluation height. The impact of subsidence on ET-*VPD* hysteresis as shown in the Figure 3.11 can also be reproduced with the conceptual model for ET (Equation 1.12), by increasing afternoon *VPD* proportionally to the changes shown in Figure 3.11 and keeping r_s identical (result not shown). However, as the observed changes in *VPD* lie well within the modelling uncertainty, the impact is not significant enough to quantify them. And a more elaborate model must be used to investigate whether the impact of subsidence on ET-*VPD* hysteresis is indeed a persistent effect.

3.3.4. Boundary Layer State: Entrainment

The second BL effect under investigation is entrainment of heat and moisture. The sensitivity to entrainment is investigated by varying the 6:00 strength of the inversion layer between the BL and RL. The weakest inversion is defined as $\Delta\theta$ = 1 K and Δq = 0 kg kg^{-1}; the strongest as $\Delta\theta$ = 4 K and Δq = -5.10^{-3} kg kg^{-1}; corresponding to $\Delta\theta_v$ ranging from 1.0 to 3.1 K. The forcing steps are specified in Table 2.2. For the reference case $\Delta\theta$ = 4 K, Δq = -1.4.10^{-3} kg kg^{-1}, and $\Delta\theta_v$ = 3.8 K.

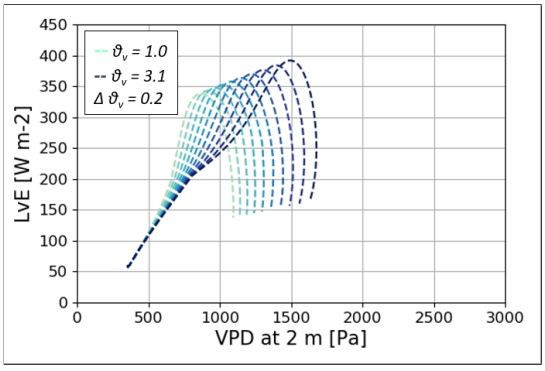

Figure 3.12: Sensitivity analysis: Impact of entrainment on ET-*VPD* hysteresis, via variation in magnitude of the RL to BL temperature and specific humidity jumps. From light to dark blue the curves represent the cases from weak ($\Delta\theta$ = 1 K and Δq = 0 kg kg^{-1}) to strong ($\Delta\theta$ = 4 K and Δq = -5.10^{-3} kg kg^{-1}) jumps. At each increment the variables respectively change 0.4 K and -5.10^{-6} kg kg^{-1}.

A stronger inversion in terms of $\Delta\theta_v$ leads to reduced morning values of w_e (Equation 2.3). Resulting in the onset of rapid BL growth being delayed (Equation 2.1), and lower BL height values throughout the entire day. At the same time, the entrained air becomes progressively warmer and more dry. As the inversion becomes stronger, the combined effect of relatively warmer air being entrained from the RL (a larger $\Delta\theta$) and a lower BL height result in an increased $\bar{\theta}$ (Equation 2.5). As in this sensitivity study the initial conditions for $\Delta\theta$ and Δq are varied together, a stronger inversion also results in relatively

more dry air being entrained, leading to a reduced $\bar{q}$ (Equation 2.7). *VPD* increases: The increased temperature results in a higher saturation pressure via the Clausius-Clapeyron relation, which is further amplified by the lower q (Equation 1.1).

The effect of a larger $\Delta\theta_v$ on L_vE and *VPD* is clearly visible in Figure 3.12. Between the weakest and the strongest inversion L_vE increases with 50 W m^{-2} due to the stronger atmospheric moisture demand (Equations 2.14 - 2.16). As L_vE is increased, H is decreased with the same amount via the surface energy partitioning (Equation 2.13). However, the initial slope of the hysteresis loop remains similar under varying initial conditions. This is caused by the net impact of surface and entrainment fluxes leading to similar morning *VPD* and L_vE. If we only look at temperature effects: (1) Under a weak inversion BL growth starts earlier, and warm air is entrained into the BL (Equations 2.3 and 2.5); the morning impact of H on $\bar{\theta}$ (Equation 2.5) is limited as the heat is divided over a larger BL height (Equation 2.1). (2) Under a strong inversion the onset of BL growth is delayed and entrainment of warm air can be neglected in the early morning; H on the other hand results in an increased $\bar{\theta}$ as the BL height remains approximately constant (Equation 2.1). Hence, both weak and strong inversion effectively lead to similar morning *VPD* and L_vE values. The same argument holds for specific humidity and its impact on *VPD* and L_vE - where its effect is smaller than that of temperature. After approximately 8:00 the BL grows under all imposed forcings, explaining the differentiation in ET-*VPD* slopes after 8:00.

The vegetation resistance r_s (not shown) is not significantly affected by changes in entrainment. This can be understood from the impact entrainment has on the surface heat fluxes and corresponding ML quantities: As described in the previous paragraph, an increase in entrainment of warm dry air leads to a decrease in $\bar{q}$ and increase in $\bar{\theta}$, and thus to an increase in saturation specific humidity. This leads to a minor increase in L_vE (Equations 2.14-2.16). As L_vE increases, H decreases, which in turn leads to a lower $\bar{\theta}$ (Equation 2.5), which dominates the previous $\bar{\theta}$ increase. From the surface energy balance, a combined decrease H and $\bar{\theta}$ may lead to θ_s remaining the same, as confirmed by the model output. A similar argument

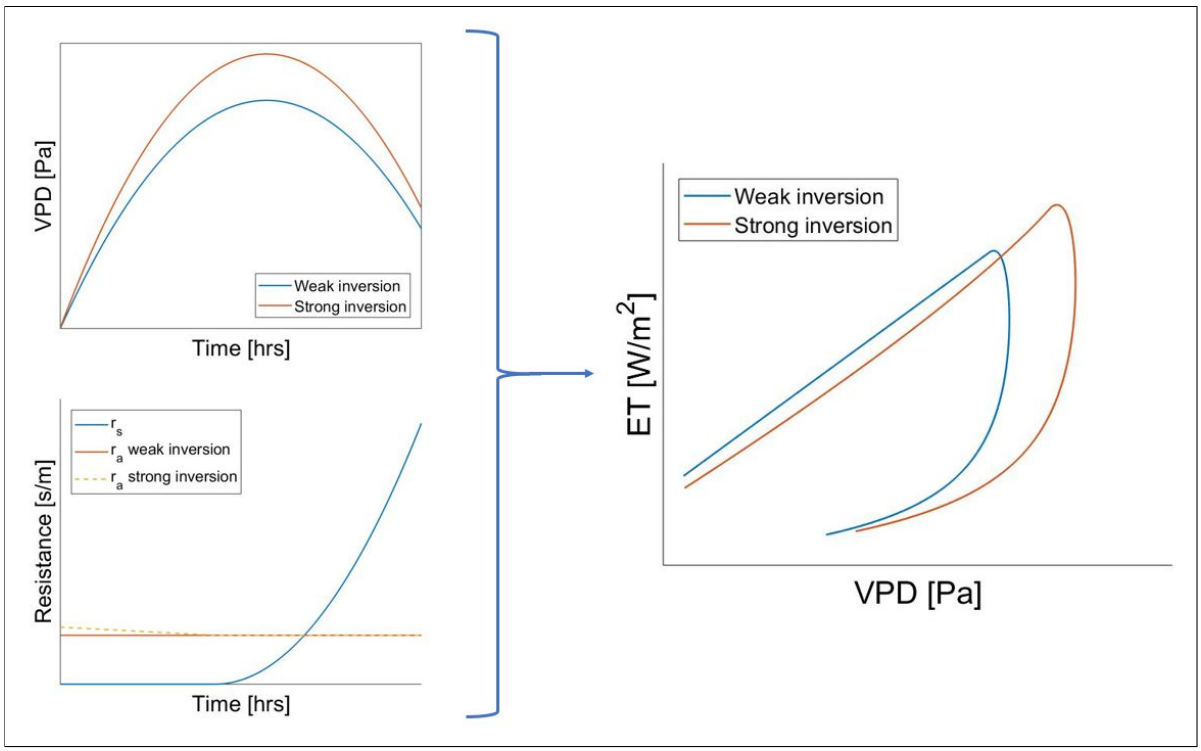

Figure 3.13: Conceptual model simulating impact of entrainment in terms of inversion strength. Upper left: *VPD* for the cases with weak and strong inversion . Lower left: Idealized diurnal courses for aerodynamic (r_a) and canopy resistances (r_s). Right: The resulting ET-*VPD* curves.

holds for L_vE, $\bar{q}$, and Equations 2.14-2.16, resulting in q_s also remaining approximately constant. Therefore, leaf level *VPD* is not significantly impacted and the vegetation feels little of entrainment variations.

The impact of changes in inversion strength on ET-*VPD* hysteresis is explained with the conceptual model for ET (Figure 3.13). Again the diurnal courses for r_a and r_s are simplified, as discussed in Chapter 3.3.1. Here early morning r_a is increased: With a stronger inversion $\Delta\theta_v$, morning ω_e decreases (Equation 2.3) and the BL growth is reduced (Equation 2.1). The reduced BL height leads to an increase in $\bar{\theta}$ (Equation 2.5), and subsequently to a decrease in H (Equation 1.11). Similarly the reduced BL height leads to an increase in $\bar{q}$ (Equation 2.7), and subsequently to a decrease in L_vE (Equations 2.14-2.16). The combined result of these two effects is that $\overline{w'\theta_v'}$ decreases (Equation 2.4), which leads to an increase of morning r_a via C_s (Equation 2.17). The combined impact of higher diurnal values for *VPD* and reduced early morning mixing (increased r_a) result in a slightly tilted hysteresis loop with higher maximum *VPD* and L_vE.

3.3.5. Turbulent Mixing

The analysis in Chapters 3.3.1-3.3.4 demonstrate that the turbulent mixing impacts ET-*VPD* hysteresis. r_a incorporates both the effects of mixing due to wind (by U) and atmospheric stability - via C_s - due to changes in for example canopy height (Equation 2.17). As mixing decreases, r_a increases, and hence ET reduces (Equations 2.14-2.16) - and vice versa. The impact of r_a on ET-*VPD* shape is investigated here, where r_a is increased from its default values with up to a Δr_a = +50 s m^{-1} change. The results are shown in Figure 3.14.

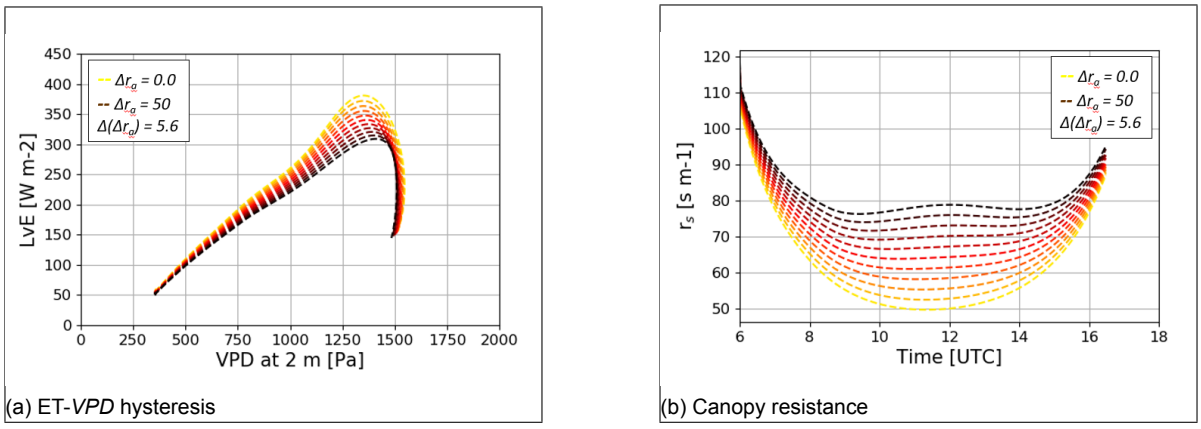

(a) ET-*VPD* hysteresis (b) Canopy resistance

Figure 3.14: Sensitivity analysis: Variation in aerodynamic resistance. From yellow to brown the curves represent the cases from no (Δr_a = 0 s m^{-1}) to substantial additional resistance (Δr_a = 50 s m^{-1}). (a) ET-*VPD* hysteresis; (b) r_s.

Throughout the day, both the hysteresis shape and r_s show a significant impact of changes in r_a (Figure 3.14), even for the smallest forcing. Without additional forcing, r_a and r_s are comparable (Figure 3.7); however, at Δr_a = 50 s m^{-1}, r_a is 120 s m^{-1} at the diurnal minimum and well exceeds r_s. As r_a is increased, r_s progressively increases (Figure 3.14b). This is explained by surface effects: Via the energy partitioning reduced mixing results in a significantly higher θ_s (over 5 K at the diurnal maximum for Δr_a = 50 s m^{-1}). The elevated θ_s leads to an increase in *VPD* at the surface - via the saturation pressure (Equation 1.1) - both of which induce stress on the vegetation: The stress results in a higher r_s, and hence reduced L_vE. This in turn results in a lower q_s. The reduction in q_s leads to a lower 2 m q via the SL parameterization, whereas the 2 m θ only minimally increases - thus leading to an overall slight decrease of 2 m *VPD*. The changes in ET-*VPD* shape are therefore driven by the impact of turbulent mixing on θ_s, and subsequently on L_vE. Here it should be noted that changes in H are negligible with respect to those in L_vE, which is possible due to a concurrent increase in G (Equation 2.13).

As the impact of r_a forcing is visible on L_vE and *VPD*, also the initial slope of the hysteresis curves is affected. The slope progressively decreases as r_a is further offset, as shown in Figure 3.14a. These effects can again be explained with the conceptual model for ET, where the diurnal courses for r_a and r_s are simplified. When a higher r_a and the resulting lower diurnal amplitude for *VPD* are imposed on the model, the resulting ET-*VPD* hysteresis curves are restricted both in ET as well as *VPD*, as shown in Figure 3.15.

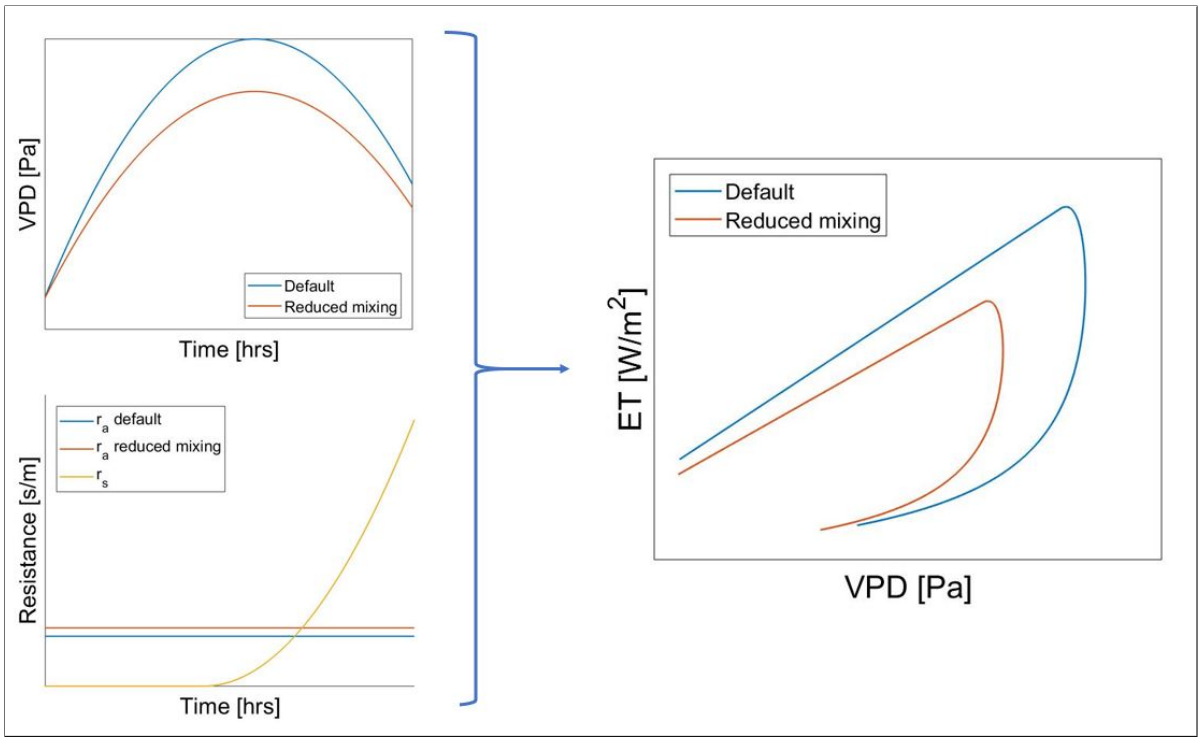

Figure 3.15: Conceptual model for ET simulating the impact of reduced mixing. Upper left: *VPD* for the cases with and without reduced mixing; the subscript *default* refers to the original r_a and *reduced mixing* to the case where r_a is artificially enhanced. Lower left: Idealized diurnal courses for aerodynamic (r_a) and canopy resistances (r_s). Right: The resulting ET-*VPD* curves.

4

Discussion

Changes in surface state, BL state, and synoptic forcing each leave their own distinct signature on ET-*VPD* hysteresis. Observations alone are unable to conclusively attribute their respective impacts (Chapter 3.1). Therefore, a prognostic modelling approach is used to set up an observation-constrained reference case that reproduces ET-*VPD* hysteresis and its underlying non-linear dynamics (Chapter 3.2). With this reference case, a sensitivity study is performed to investigate the influence of selected states and forcings (Chapter 2.7) on hysteresis appearance (Chapter 3.3). Inversely, deducing the strength of each effect from the shape of a single curve is complex as their impacts can convolute. Quantification of hysteresis shape allows for speculation on how to distinguish between the studied effects.

Quantification

To explore the potential and limitations of the chosen metrics (Chapter 2.7), the imposed variations and their respective impacts are quantified in Figure 4.1. The horizontal axis represents varying initial conditions, as specified in Table 2.2. The figure shows that changes in soil moisture (represented by the soil moisture availability fraction *f(w)*; yellow squares) and the vegetation's capacity to assimilate CO_2 for photosynthesis ($A_{m,max,298}$; blue diamonds) have a similar impact on hysteresis shape. The two senescence effects are indistinguishable unless either soil moisture or leaf gas exchange is known from observations. As *f(w)* or $A_{m,max,298}$ decreases, the stomata close and r_s increases over an order of magnitude. This leads to a maximum decrease in L_vE of 300 W m^{-2}. Concurrently, the diurnal *VPD* width increases with of up to 1000 Pa. Consequently, the initial slope of the hysteresis curve is reduced from 0.3 to almost 0 W m^{-2} Pa^{-1}. Therefore showing the strong BL feedbacks in response to surface changes.

When progressively warmer and dryer air is entrained (via changes in the inversion strength $\Delta\theta_v$ between BL and residual layer, red triangles), the impacts of changing BL height, turbulent fluxes, and ML quantities cancel each other out at the surface, leaving surface temperature and specific humidity approximately unaffected. Consequently, the stomatal aperture is unchanged, showing surface feedbacks can be neglected. The diurnal maximum for L_vE only increases up to 70 W m^{-2}, primarily due to changes in ML specific humidity. *VPD* width changes with up to 750 Pa. The impact of entrainment on L_vE and *VPD* results in a ET-*VPD* slope variation of over 0.3 W m^{-2} Pa^{-1}, which is comparable to senescence induced slope changes.

Synoptic forcing (subsidence due to large-scale horizontal wind divergence *div(U)*, green circles) has negligible impact on ML and surface quantities. None of the metrics shows significant change within the model uncertainty. Subsidence can therefore not be derived from ET-*VPD* shape changes.

No quantification is given for changes in turbulent mixing, as r_a is forced with a continuously imposed offset, rather than as an initialization condition. Therefore, the feedback of

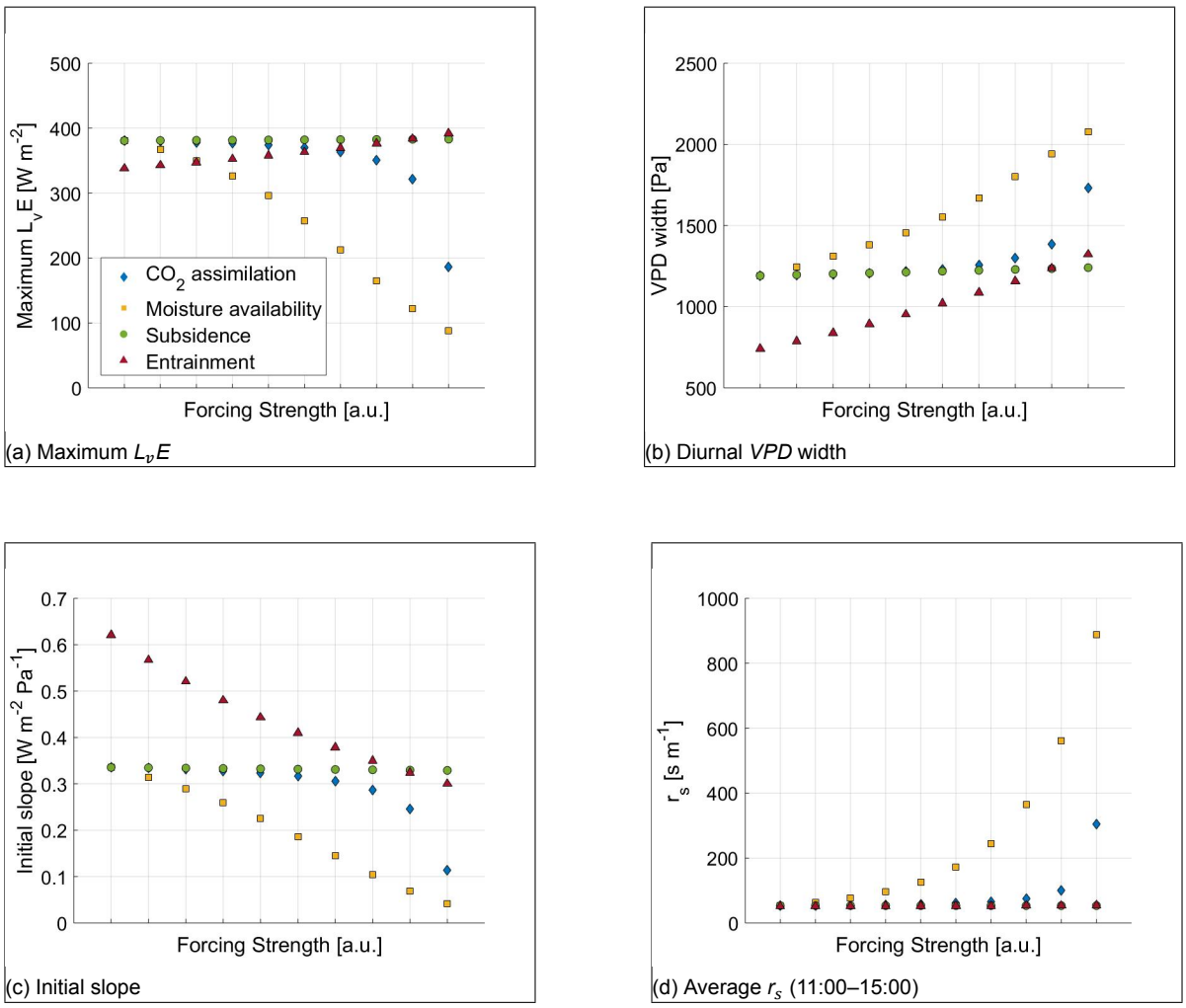

Figure 4.1: Impact of changes in surface and BL states on ET-*VPD* hysteresis appearance: (a) Maximum L_vE; (b) Maximum diurnal change in *VPD*; (c) Initial slope; (d) Average afternoon r_s (11:00 - 15:00 average). Yellow squares represent changes is soil moisture function *f(w)*, which ranges from left to right from 1 to 0 [-]; Blue diamonds changes in the vegetation's capacity to assimilate CO_2, which ranges from left to right from an $A_{m,max,298}$ of 1.98 to 0.04 mg m^{-2} s^{-1}; Green circles changes in w_s from a *div(U)*, which ranges from left to right from 0 to 1.10^{-5} s^{-1}; Red triangles changes in entrainment from an inversion strength, varying from $\Delta\theta$ = 1 K and Δq = 0 kg kg^{-1} to $\Delta\theta$ = 4 K and Δq = -5.10^{-3} kg kg^{-1}, corresponding to an effective $\Delta\theta_v$ variation from 1.0 to 3.1 K. The horizontal axis represents the relative position between the two extremes of each varied quantity; the respective values the quantities are summarized in Table 2.2.

surface and atmospheric processes on r_a is not accounted for and caution is needed quantifying the modelled ET-*VPD* changes. However, the overall effect of r_a can still be deduced. Under increased r_a, the afternoon average for r_s increases and L_vE decreases. *VPD* is only affected to a minor extent due to competing effects of temperature and moisture (Equation 1.1) at the evaluation height.

The discussion shows that changes in entrainment of warm, dry air (θ_v) and senescence may have similar impacts on the initial slope of the hysteresis curve and diurnal *VPD* width. Their respective impacts on ET are distinct, which allows for the disentanglement of entrainment and senescence effects. However, modest variations in the diurnal L_vE maximum - in the order of tens of W m^{-2} - may also result from a superposition with turbulent mixing induced changes. In addition, typical time scales may help unravel the contributions of entrainment and senescence: Senescence generally varies on weekly to monthly time scales whereas initial inversion strength and turbulent mixing can vary over days or even hours. Thus, entrainment effects can be separated from those of senescence, provided the observed changes have sufficient amplitude.

The proposed approach for resolving entrainment and senescence impacts from ET-*VPD* hysteresis shape changes can thus be applied when: (1) The reference case reflects the soil, vegetation type, approximate meteorological conditions, and surface heterogeneity; (2) The day is cloud free; and (3) if the investigated hysteresis signature is larger than the model errors and the impact of possible turbulent mixing effects. To generalize the interpretation of hysteresis shape to changes in all surface and BL variables and forcings - e.g. advection, shifted initial profiles for θ and q, vegetation species - the impact of these remaining effects needs to be investigated. Here, several variables are suspected to have similar impact on hysteresis shape: For example, advection of warm, dry air may be difficult to distinguish from entrainment. Similarly, a significant offset in temperature or specific humidity may cause changes in stomatal aperture comparable to that of soil moisture induced vegetation stress.

Relation to Previous Work

Due to the different, case-specific setups between the present study and earlier reported studies (Table 1.1) a direct comparison of the results is not straightforward. However, this thesis confirms the influence of most variables identified in earlier studies. Secondly, although identifying key driving mechanisms remains impossible with observations alone, the CloudRoots data set offers an improved analysis foundation compared to earlier work, as it spans all scales of interest, from soil to lower troposphere, and covers not only meteorology but also hydrology and biology.

The feedbacks between surface and atmosphere are an important factor in setting the diurnal ET-*VPD* hysteresis shape (described in Chapter 3.3), showing that modelling needs to incorporate these feedbacks. Although Zhang et al. (2014) are successful in attributing the response of surface states to a specific BL forcing with their uncoupled diagnostic model, their surface-BL system has limited applicability. The prognostic model proposed in this thesis is coupled, thus allowing for a systematic identification of key drivers of ET-*VPD* hysteresis over a wide range of realistic conditions. Furthermore, the model successfully incorporates essential biological behaviour, and therefore progresses the state-of-the-art.

Alternatively, Van Heerwaarden et al. (2010) use the time derivative of the Penman equation to evaluate the relative impacts of forcings and feedbacks on ET. They conclude that *"Surface layer feedbacks are negligible in fully coupled systems"*; which is confirmed for the case of changes in BL state. Although thorough, their approach is involved, whereas comparing modelled and observed ET-*VPD* hysteresis can offer a simple and rapid framework for assessing key changes in BL and surface states. Furthermore, they use a semi-empirical vegetation model rather than the mechanistic A-r_s representation for stomatal response. Notwithstanding, their approach is rigorous and can aid the understanding of observed ET-*VPD* effects.

Further Implications

- Surface-atmosphere coupling is essential in atmospheric modelling. By looking at surface conditions alone, non-linear dynamics are neglected and feedbacks driving stomatal adaptation may be missed.
- Under cloud-free conditions, variations in soil moisture stress largely determine ET. Therefore, to improve ET in weather and climate modelling, it is essential to optimize soil moisture estimates. Conversely, ET-*VPD* hysteresis can be used to estimate soil moisture stress from observations, offering a rapid assessment tool for constraining soil moisture estimates.
- Both observations and modelling show that the hysteresis amplitude - in terms of differences between morning and afternoon ET for similar *VPD* - typically lies in the order of 100 - 300 W m^{-2}. Therefore, it is essential to correct the assumption of a linear ET-*VPD* relation over vegetated surfaces in hydrological models. Doing so will offer a significant improvement to water availability estimates.

5

Conclusion

This thesis aims to investigate how surface and atmospheric processes control evapotranspiration (ET). ET is a key driver for the the water cycle, surface energy balance, as well as many biochemical reactions. However, it still remains a major modelling uncertainty. To improve our understanding of ET, the hysteretic diurnal relationship between ET and the atmospheric moisture demand in terms of vapor pressure deficit (*VPD*) is used to analyse and quantify the impacts of various changes in surface and BL state. To do so, mixed-layer (ML) modelling is combined with the CloudRoots data set; the data set covers meteorology, hydrology, and biology and spans all scales of interest, from surface to lower troposphere. With the ML model the proof-of-concept is delivered for realistically modelling ET-*VPD* hysteresis, and a sensitivity study is performed in order to answer the research question:

Can the characteristics of ET-*VPD* hysteresis uncover and quantify the contributions of surface and atmospheric processes in controlling ET?

The three research steps are carried out:

1. *Observations: Analysis of the 2018 CloudRoots campaign data*

   The time series of diurnal ET-*VPD* hysteresis loops shows a seasonal evolution of the initial angle of the curves, as well as of maximum ET and *VPD* width. This evolution can be linked to stomatal regulation in response to vegetation senescence. In addition, further fluctuations in maximum ET and diurnal *VPD* range are observed, which can only be partly linked to individual surface or near-surface variables. Therefore large-scale BL effects such as entrainment impact hysteresis appearance. As observations alone are unable to explain all measured variations of ET-*VPD* hysteresis, modelling is essential to identify the drivers of hysteresis shape.

2. *Modelling: Proof-of-concept and reference case*

   A coupled, prognostic ML model is used that incorporates a mechanistic surface response to soil and atmospheric conditions. The model is improved in terms of leaf level vapor pressure deficit and surface layer temperature and pressure. In addition the model is adapted to take into account the morning residual layer to free troposphere transition, and surface heterogeneity is incorporated by allowing the sensible heat flux to be in line with its landscape aggregate. Observations from a reference day with no vegetation stress and turbulent mixing conditions are used for parameter initialization and evaluation. For all variables the diurnal evolution is reproduced, from turbulent heat fluxes to boundary layer height, reflecting the validity of the underlying dynamics of the model. The resulting hysteresis curve corresponds with the observations and realistically reflects surface-atmosphere interactions and vegetation biology. This result delivers for the first time a proof-of-concept for prognostically modelling ET-*VPD* hysteresis with a ML model. Therefore offering a novel framework for the investigation of ET-*VPD* hysteresis.

3. *Modelling: Sensitivity analysis*

   For the sensitivity analysis, the impacts of soil moisture availability, the vegetation's capacity to assimilate CO_2 for photosynthesis, entrainment of relatively warm and dry air, subsidence, and turbulent mixing, on hysteresis appearance are investigated. The following can be concluded for cloud free days that have comparable atmospheric conditions:

   - An increase in surface stress is reflected by a combined decrease in latent heat flux and increase in *VPD*, thus also leading to a decreasing initial ET-*VPD* slope. The effects of **soil moisture availability** and vegetation **capacity to assimilate CO_2** for photosynthesis are indistinguishable from the hysteresis curves alone. Additional soil moisture measurements will allow for the unraveling of these two effects.
   - An increase in inversion strength - affecting **entrainment** and leading to a stronger warming and drying tendency of the BL - is characterised by an increase in *VPD* combined with a modest increase in L_vE. Thus showing a different fingerprint than for senescence.
   - Changes in **subsidence** have no impact on either the appearance of ET-*VPD* hysteresis or the stomatal response.
   - Increased wind speed or decreased vegetation height enhances **turbulent mixing**. This affects stomatal aperture and L_vE, albeit that the magnitude of the changes is lower than for senescence or entrainment effects. It has little impact on *VPD* due to competing effects of surface temperature and moisture.

The ultimate goal to which this study contributes, is to derive how the state of the surface and atmosphere control ET *from a single hysteresis curve*. Entrainment and senescence have their own characteristic hysteresis fingerprint, and their respective contributions can be unraveled. As variations in turbulent mixing also affect ET, they limit the interpretation of modest shape changes. However, on a day-to-day and even week-to-week basis, the assumption of constant soil moisture and photosynthetic capacity may be justified, and changes in hysteresis shape are primarily caused by entrainment. Additionally, stomatal behaviour can conclusively separate surface and entrainment effects.

To conclusively interpret the observed ET-*VPD* shape changes, surface and BL states beyond those described - e.g. initial temperature profile or advection of warm, dry air - need to be investigated. Although unravelling *all* key driving factors of ET-*VPD* hysteresis shape will likely prove impossible, including typical time scales will help separate factors and dominant drivers are likely to emerge. Therefore, combining ET-*VPD* hysteresis observations and modelling offers a promising tool to map changes in BL and surface states.

6

Recommendations

1. **Biological observations** show that the default parameters in the mechanistic vegetation model are not rigid. This is confirmed by the founding work of Jacobs (1994), who reports changes in default values due to environmental adaptation of the vegetation. Therefore, including extensive biological observations in measurement campaigns will allow for better initialization of the A-r_s model, as well as for investigation of the validity of the model's assumptions.
2. Landscape heterogeneity is the rule rather than the exception. This heterogeneity results in different turbulent fluxes for the measurement site and surrounding area; where the aggregate of all turbulent fluxes determines BL evolution. The contrast between field scale and landscape scale fluxes can be incorporated by using **Large Eddy Simulation**. If the more rapid method of ML modelling is used, heterogeneity can be incorporated by introducing **tiling** in the CLASS ML model. For tiling, conceptually a homogeneous field tile is linked to a separate landscape tile, where the landscape acts as a dynamically evolving boundary condition to the field. Thus the landscape aggregate setting BL growth and advection can be accounted for.
3. **Dimensional analysis** may shed further light on the appearance of ET-*VPD* hysteresis, and therefore also on the controlling factors of ET. In addition it can indicate appropriate metrics for the quantification of ET-*VPD* shape changes. However, it should be noted that as a large number of initial conditions impact hysteresis shape, uncovering the exact ratios of the quantities at play may prove complex.
4. Last, a much wider range of initial conditions than those investigated will influence ET-*VPD* hysteresis shape:
    - To study the impact of **entrainment**, variations in $\Delta\theta$ and Δq need to be studied independently. Both quantities impact the inversion strength $\Delta\theta_v$, and subsequently the entrainment velocity and BL growth. Furthermore, their respective impacts on ML temperature and specific humidity will have a different impact of ET-*VPD* hysteresis.
    - Observations indicate that early morning **clouds** are likely to truncate hysteresis loops both in ET as well as *VPD*. Whereas an immediate impact from clouds is expected, it is remarkable that their impression persists throughout the day.
    - The effect of advection of warm, dry air into the ML will most likely be similar to that of entrainment. And the impact of a significant offset in initial temperature or specific humidity may be comparable to that of soil moisture stress. Investigating the influence of the **remaining initial conditions** is a prerequisite for using ET-*VPD* hysteresis to unravel the impact of surface and BL states on ET. Here conditions should both be varied as a single controlling parameter as well as in coupled configurations.

A

Model Adaptations

The CLASS ML model was updated to include (1) the morning RL to FT transition, (2) an improved parameterization for the leaf level *VPD*, and (3) an improved parameterization for surface layer temperature and pressure.

A.1. Morning Transition

Coupled to the BL evolution are the respective jumps and lapse rates of scalar quantities at the top of the ML. Early in the morning the BL is topped by the RL. As the ML grows, heat and humidity from the RL are entrained according to the ML growth rate, and respective jumps and lapse rates of the scalars. This continues until the ML reaches the FT and humidity and heat are entrained from the FT. This transition from RL to FT is called the *morning transition*, and needs to be accounted for in the model. Therefore, at model initialization each scalar k requires a set initial jump between ML and RL Δk_{RL} as well as its corresponding RL lapse rate $\gamma_{k,RL}$. And the same hold for the FT with jump Δk_{FT} between RL and FT, and lapse rate $\gamma_{k,FT}$. The ML, RL, and FT with said jumps and lapse rates is visualised schematically in figure A.1.

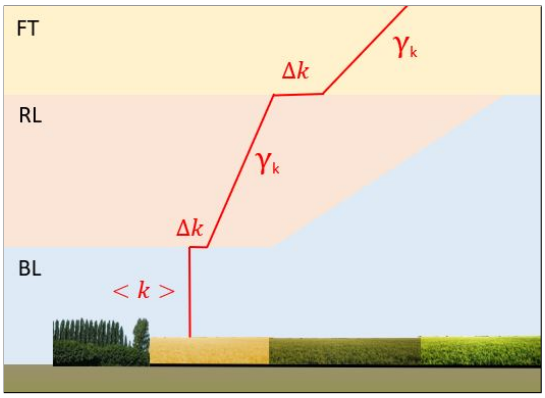

Figure A.1: Schematic depiction of the differences in jump and lapse rate between RL and FT for a scalar *k*. <*k*> denotes the ML value, Δk the discrete jump between two adjacent layers, and γ_k the lapse rate in either the RL or FT.

In the original model, the jump and lapse rate are set as FT boundary conditions. As the ML grows, the lapse rates remain constant whereas the jumps change according to equations 2.8 and 2.6. To incorporate both the RL and FT properties, the model is updated:

- For the reference day, the Joyce data is used to check the height and time of the RL to FT transition. The FT is conveniently reached around 12:00, the time of the second radiosonde measurement.
- The initial Δq, γ_q, $\Delta\theta$, and γ_θ are derived from the 00:00 radiosonde data, and are set as the RL boundary condition in the model.
- Once the modelled ML reaches the height of the RL to FT transition:
  - The $\Delta\theta$ jump is increased so that the new value matches Δ_θ measured for the FT at 12:00; γ_θ is set to the FT value.

– For the FT Δq is not a (semi-)discrete jump but rather a transition zone that extends over more than 500 m, continuing well above the final ML height. Thus, the $\gamma_{q,FT}$ is set to correspond to that of the transition zone. As at the transition time, the remaining Δq_{RL} is very low, it is left as is.

A.2. Leaf Level Vapor Pressure Deficit

In the original CLASS model the leaf level *VPD* (D_s) in the A-r$_s$ module is parameterized as:

$$D_s = e_{sat}(T_s) - e_{SL,top} \tag{A.1}$$

Where *SL,top* denotes the state at the top of the SL. However, mechanistically the vegetation is insensitive to the difference between e_{sat} at the surface and at the vapor pressure at level of the SL top $e_{SL,top}$, but rather to the *VPD* at the surface itself. The parameterization is thus redefined as:

$$D_s = e_{sat}(T_s) - e_{a,surface} = e_{sat}(T_s) - \frac{q_s P_s}{0.622} \tag{A.2}$$

where equation 1.4 is used, P_s is the pressure at the surface, and 0.622 the ratio between the gas constants for dry air and water vapor.

Correcting the *VPD* at leaf level yields a significant change in the diurnal evolution of all fluxes and scalars. The impact for e.g. L_vE is approximately 100 W/m^2 at the maximum for the reference day, which amounts to a change of about 20%.

A.3. Surface Layer Temperature and Pressure

Formally the ET components are parameterized according to 2.14, 2.15, and 2.16. In CLASS this is implemented as

$$L_vE = -\frac{\rho L_v}{r_a + r_s}(q - (s(T_s - T_{SL,top})) + q_{sat,surface}) \tag{A.3}$$

Where s is the slope of the Clausius-Clapeyron saturation curve. It is assumed that $T_{SL,top} = \theta_{SL,top}$ and $P_{SL,top} = P_{surface}$. As the surface layer extends up to 150 m for the reference day, the assumptions no longer hold. The temperature and pressure are therefore corrected for the dry adiabatic lapse rate:

$$T_{SL,top} = \theta_{SL,top} - \frac{g h_{SL,top}}{c_p} \tag{A.4}$$

$$P_{SLtop} = P_{surface} - \rho g h_{SL,top} \tag{A.5}$$

The impact from the corrected temperature and pressure at the top of the surface layer is minimal, yielding to a change in e.g. L_vE of 20 W/m^2 at the diurnal maximum of the reference day. A value that is within the measurement error of the EC.

B

Model Initialization

B.1. Model Parameters

ML Model Parameters		
Parameter [Units]	**Value**	**Source**
Time step [s]	60	-
Runtime [s]	50400	-
h_{RL} [m]	135	Joyce microwave
h_{FT} [m]	1400	radiosonde
P_s [Pa]	100600	EC pressure gauge
div(U) [s^{-1}]	0	default
f_c [m s^{-1}]	1.10^{-4}	latitude
β [-]	0.2	default
$\bar{\theta}$ [K]	286.2	profile data and radiosonde
$\Delta\theta_{RL}$ [K]	4	radiosonde
$\Delta\theta_{FT}$ [K]	4.4	radiosonde
$\gamma_{\theta,RL}$ [K]	$4.9.10^{-3}$	radiosonde
$\gamma_{\theta,FT}$ [K]	$6.2.10^{-3}$	radiosonde
adv_θ [K]	[-]	see section B.3
$\bar{q}$ [kg kg^{-1}]	[-]	see section B.3
Δq_{RL} [kg kg^{-1}]	$-1.4.10^{-3}$	radiosonde
$\gamma_{q,RL}$ [kg kg^{-1} m^{-1}]	$-2.7.10^{-6}$	radiosonde
$\gamma_{q,FT}$ [kg kg^{-1} m^{-1}]	$-9.0.10^{-6}$	radiosonde
adv_q [kg kg^{-1} s^{-1}]	0	default
$\overline{CO_2}$ [ppm]	400	profile measurements
ΔCO_2 [ppm]	-44	profile measurements
γ_{CO2} [ppm m^{-1}]	0	default
adv_{CO2} [ppm s^{-1}]	0	default
u [m s^{-1}]	1.75	profile measurements
Δu [m s^{-1}]	3	profile measurements
γ_u [m s^{-2}]	$-1.8.10^{-3}$	profile measurements
adv_u [m s^{-2}]	0	default
v [m s^{-1}]	0	default
Δv [m s^{-1}]	0	default
γ_v [m s^{-2}]	0	default
adv_v [m s^{-2}]	0	default
u* [m s^{-2}]	0.3	EC
z_{0m} [m]	0.02	canopy height
z_{0h} [m]	0.002	canopy height

Latitude [deg]	50.9	geographical location
Longitude [deg]	6.4	geographical location
Day-of-year [days]	127	date selected case
Start time [hrs UTC]	6.0	[-]
Cloud cover faction [-]	0	camera
dF_z [W m^{-2}]	0	camera
SM top soil layer [m^3 m^{-3}]	0.177	soil measurements
SM deep soil layer [m^3 m^{-3}]	0.286	soil measurements
Vegetation cover fraction [-]	0.98	visual inspection, camera
T top soil layer [K]	285.5	soil measurements
T deep soil layer [K]	284	soil measurements
Clapp & Hornb. param. a [-]	0.219	soil composition
Clapp & Hornb. param. b [-]	5.3	soil composition
Clapp & Hornb. param. a [-]	4	soil composition
CG_{sat} [-]	$3.56.10^{-6}$	soil composition
w_{sat} [m^3 m^{-3}]	0.472	soil composition
w_{fc} [m^3 m^{-3}]	0.3	soil composition
w_{wilt} [m^3 m^{-3}]	0.154	soil composition
$C1_{sat}$ [-]	disabled	soil composition
$C2_{ref}$ [-]	disabled	soil composition
LAI [-]	4.5	on-site determination
g_D [-]	0	vegetation height
$r_{s,soil,min}$ [s m^{-1}]	50	default
α [-]	0.2	radiation measurements
T_s [K]	286.3	profile measurements
W_{max} [m]	0.0002	default
W_{liq} [m]	0.0001	on-site observations
Λ [-]	5.9	default

A-r_s Model Parameters		
Parameter [Units]	**Value**	**Source**
Γ [mg m^{-3}]	68.5	C3 reference value
$Q10_{CO2}$ [-]	1.5	C3 reference value
$g_{m,298}$ [mm s^{-1}]	10.0	leaf gas exchange
$A_{m,max,298}$ [mg m^{-2} s^{-1}]	1.926	leaf gas exchange
T_{1gm} [K]	278	C3 reference value
T_{2gm} [K]	301	C3 reference value
$Q10_{A,m,max}$ [-]	2.0	C3 reference value
$T_{1A,m,max}$ [K]	281	C3 reference value
$T_{2A,m,max}$ [K]	311	C3 reference value
f_0 [-]	0.89	C3 reference value
a_d [kPa^{-1}]	0.07	C3 reference value
α_0 [mg J^{-1}]	0.0053	leaf gas exchange
K_x [m m^{-1}]	0.7	C3 reference value
$g_{min,c}$ [mm s^{-1}]	$2.5.10^{-4}$	C3 reference value

B.2. Forced Quantities

Heat is advected for every time step throughout the entire run of the model. This is done to mimic the impact of the combined landscape H setting the growth of the ML height and temperature. The amount is proportional to the diurnal evolution of H contrast between the study site and neighbouring field with bare soil (Miranda García, 2019). The values of adv_T that are used to force the model are given by:

$$adv_T = 2.5.10^{-4}.e^{-\frac{(time[UTC]-12)^2}{5}} \tag{B.1}$$

and are shown in figure B.1a.

Similarly $\bar{q}$ is forced for the 6:00 - 8:00 period. This is done to compensate for the differences in mixing between the observations and modelled quantities in the near-surface layer. $\bar{q}$ is forced in such a way that the modelled 2 m value for q matches those of the profile measurements. The values of q that are used to force the model are given by:

$$q = 0.0067 - 0.0004(time[UTC] - 6.5) \tag{B.2}$$

and are shown in figure B.1b.

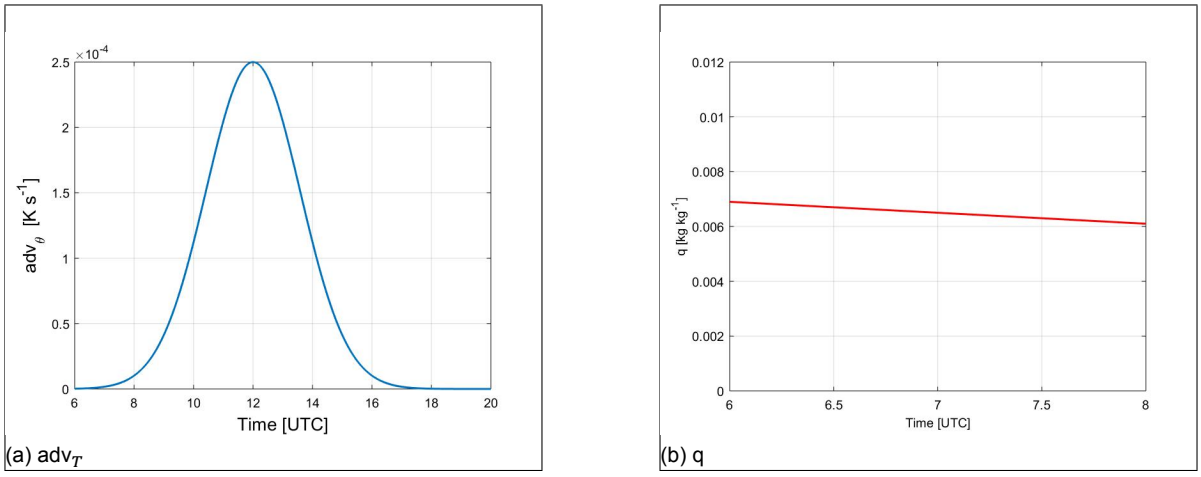

Figure B.1: Quantities forced in the model. (a) Advection of heat; (b) Specific humidity.

C

Variables and Acronyms

Symbol	Variable	Units
A	assimilation rate for CO_2	mg m^{-2} s^{-1}
A	ratio of the entrainment to surface kinematic buoyancy fluxes	[-]
adv_{CO2}	advection of CO_2 into the ML	ppm s^{-1}
adv_q	advection of specific humidity into the ML	kg kg^{-1} s^{-1}
adv_u	advection of longitudinal wind into the ML	m s^{-1} s^{-1}
adv_v	advection of latitudinal wind into the ML	m s^{-1} s^{-1}
adv_θ	advection of heat into the ML	K s^{-1}
a_d	regression coefficient to calculate the ratio between the leaf and external CO_2 concentration	[-]
$A_{m,max}$	maximum assimilation rate for CO_2	mg m^{-2} s^{-1}
$A_{m,max,298}$	maximum assimilation rate for CO_2 at 298 K	mg m^{-2} s^{-1}
α	albedo	[-]
α_0	initial low light conditions use efficiency for CO_2	mg J^{-1}
β	entrainment ratio for virtual heat	[-]
CG_{sat}	saturated soil conductivity for heat	[-]
CO_2	Carbondioxide concentration	ppm
c_{liq}	fraction of vegetation covered in liquid water	[-]
c_p	heat capacity	J K−1
C_S	drag coefficient for scalars	[-]
c_{veg}	fraction of area covered in vegetation	[-]
$C1_{sat}$	parameter to calculate top layer soil moisture tendency	[-]
$C2_{ref}$	parameter to calculate top layer soil moisture tendency	[-]
$div(U)$	large scale wind divergence	m s^{-1}
dF_z	cloud top radiative divergence	W m^{-2}
D_s	leaf level vapor pressure deficit	Pa
ΔCO_2	jump in CO_2 at the inversion layer	ppm
Δq	jump in specific humidity at the inversion layer	kg kg^{-1}
Δq_{RL}	jump in specific humidity between BL and RL	K
Δr_a	imposed forcing on r_a	s m^{-1}
Δu	jump in longitudinal wind velocity at the inversion layer	m s^{-1}
Δv	jump in latitudinal wind velocity at the inversion layer	m s^{-1}
$\Delta\theta$	jump in potential temperature at the inversion layer	K
$\Delta\theta_{FT}$	jump in potential temperature from BL to FT	K
$\Delta\theta_{RL}$	jump in potential temperature from BL to RL	K
E	evapotranspiration	kg m^{-2} s^{-1}
e_a	atmospheric vapor pressure	Pa

$e_{a,surface}$	atmospheric vapor pressure at the surface	Pa
e_{sat}	saturation vapor pressure	Pa
$e_{SL,top}$	atmospheric vapor pressure at the top of the surface layer	Pa
f_c	Coriolis parameter	m s^{-1}
f_0	maximum value of the ratio between the leaf and external CO_2 concentration	[-]
$f(\omega)$	soil moisture stress function	[-]
g	gravitational acceleration	m s^{-2}
G	ground heat flux	W m^{-2}
g_d	correction factor transpiration for VPD for high vegetation	[-]
g_m	mesophyll conductance	m s^{-1}
$g_{m,298}$	mesophyll conductance at 298 K	m s^{-1}
$g_{min,c}$	minimum cuticular conductance	mm s^{-1}
g_s	canopy conductance	m s^{-1}
γ_{CO2}	free troposphere lapse rate for CO_2	ppm^{-1} m^{-1}
γ_q	free troposphere lapse rate for specific humidity	kg kg^{-1} m^{-1}
$\gamma_{q,FT}$	free troposphere lapse rate for specific humidity	kg kg^{-1} m^{-1}
$\gamma_{q,RL}$	residual layer lapse rate for specific humidity	kg kg^{-1} m^{-1}
γ_u	free troposphere lapse rate for longitudinal wind velocity	m s^{-1} m^{-1}
γ_v	free troposphere lapse rate for latitudinal wind velocity	m s^{-1} m^{-1}
γ_θ	free troposphere lapse rate for potential temperature	K m^{-1}
$\gamma_{\theta,FT}$	free troposphere lapse rate for potential temperature	K m^{-1}
$\gamma_{\theta,RL}$	residual layer lapse rate for potential temperature	K m^{-1}
Γ	CO2 compensation concentration	mg m^{-3}
h	mixed-layer height	m
h_{FT}	height at which the free troposphere starts	m
h_{RL}	height at which the residual layer starts	m
$h_{SL,top}$	height of the top of the surface layer	m
H	sensible heat flux	W m^{-2}
K_x	extinction coefficient PAR	[-]
L	Obukhov length	m
LAI	leaf area index	[-]
L_{in}	incoming longwave radiation	W m^{-2}
L_{out}	outgoing longwave radiation	W m^{-2}
L_v	latent heat of vaporation	J kg^{-1}
L_vE	latent heat flux	W m^{-2}
L_vE_{liq}	latent heat flux for evaporation of intercepted water	W m^{-2}
L_vE_{soil}	latent heat flux for evaporation of soil water	W m^{-2}
L_vE_{veg}	latent heat flux for transpiration from plants	W m^{-2}
Λ	thermal conductivity skin layer	[-]
P	pressure	Pa
P_0	reference pressure; in this study: surface pressure	Pa
P_s	surface pressure	Pa
PAR	photosynthetically active radiation	W m^{-2}
q	specific humidity	kg kg^{-1}
q_l	liquid water content	kg kg^{-1}
q_s	surface specific humidity	kg kg^{-1}
q_{sat}	saturation specific humidity	kg kg^{-1}
$q_{sat,surface}$	saturation specific humidity at the surface	kg kg^{-1}
q_v	vapor content	kg kg^{-1}
$\overline{q}$	mixed layer specific humidity	kg kg^{-1}
Q^*	net radiation	W m^{-2}
$Q10_{A,m,max}$	function parameter to calculate maximal primary productivity	[-]
$Q10_{CO2}$	function parameter to calculate CO2 compensation	[-]
r_a	aerodynamic resistance	s m^{-1}

R_d	gas constants of dry air	J kg^{-1} K^{-1}
R_v	gas constants of water vapor	J kg^{-1} K^{-1}
r_s	canopy resistance	s m^{-1}
$r_{s,soil}$	minimum soil resistance	s m^{-1}
r_{soil}	soil resistance	s m^{-1}
ρ	air density	kg m^{-2}
ρ_w	liquid water density	kg m^{-2}
s	slope of the saturation curve	Pa K^{-1}
S_{in}	incoming shortwave radiation	W m^{-2}
S_{out}	outgoing shortwave radiation	W m^{-2}
T	temperature	K
T_a	air temperature	K
T_s	surface temperature	K
$T_{SL,top}$	temperature at the top of the surface layer	K
$T_{1A,m,max}$	reference temperature to calculate maximal primary productivity	K
T_{1gm}	reference temperature to calculate mesophyll conductance	K
$T_{2A,m,max}$	reference temperature to calculate maximal primary productivity	K
T_{2gm}	reference temperature to calculate mesophyll conductance	K
T_{2m}	temperature at 2 m	K
θ	potential temperature	K
$\bar{\theta}$	ML temperature	K
θ_a	atmospheric potential temperature	K
θ_s	surface potential temperature	K
$\theta_{SL,top}$	temperature at the top of the surface layer	K
θ_v	virtual potential temperature	K
u	wind speed in the longitudinal direction	m s^{-1}
U	absolute wind speed	m s^{-1}
$\overline{u'w'}$	turbulent momentum flux in the zonal direction	m^2 s^{-2}
u_*	surface friction velocity	m s^{-1}
v	wind speed in the latitudinal direction	m s^{-1}
$\overline{v'w'}$	turbulent momentum flux in the meridional direction	m^2 s^{-2}
VPD	vapor pressure deficit	Pa
w_e	entrainment velocity	m s^{-1}
w_{fc}	field capacity volumetric water content	[-]
w_s	velocity of large-scale subsidence	m s^{-1}
w_{sat}	saturated volumetric water content	[-]
w_{wilt}	wilting point volumetric water content	[-]
W_{liq}	equivalent water layer depth for wet vegetation	m
W_{max}	thickness of water layer on wet vegetation	m
$\overline{w'\theta'}$	heat flux	K m s^{-1}
$\overline{w'\theta'_v}$	kinematic buoyancy flux	K m s^{-1}
$(\overline{w'\theta'_v})_e$	entrainment kinematic buoyancy flux	K m s^{-1}
$(\overline{w'\theta'_v})_s$	surface kinematic buoyancy flux	K m s^{-1}
$\overline{w'q'}$	moisture flux	kg kg^{-1} m s^{-1}
z_{0h}	roughness length for scalars	m
z_{0m}	roughness length for momentum	m

Acronym	Meaning
AERI	Atmospheric Emitted Radiance Interferometer
BL	boundary Layer
CO_2	Carbondioxide
C3	plant classification based on assimilation path of CO_2 for photosynthesis, 3-phosphoglycerate is the first product
EC	Eddy Covariance
ET	evapotranspiration
FT	free troposphere
ICOS	Integrated Carbon Observation Site
IOP(s)	intensive observation period(s)
JOYCE	Jülich Observatory for Cloud Evolution
ML	mixed-layer
PAR	photosynthetically active radiation
RL	residual layer
SL	surface layer
SM	soil moisture
SPAC	Soil-Plant-Atmosphere Continuum
UTC	Coordinated Universal Time
VPD	vapor pressure deficit

D

Addendum to the Conceptual Model

To derive the conceptual model for ET (described by Equation 1.12 in Chapter 1.2.2), several assumptions are made. The first term of Equation 1.8 is neglected based on the observations for 7 May 2018, when H is small compared to L_vE (black symbols in Figure 3.2b) - with the diurnal maximum of H being less than 5% of the L_vE maximum. However, this low H is observed due to specific conditions generating an oasis effect at the measurement site, whereas for extended homogeneous surfaces H generally is of the same order of magnitude as L_vE, even for well-watered vegetation in full growth. As such, the derivation of the conceptual model for ET from Equation 1.8 poses two problems:

- The key driver of ET is the available energy, which is dominated by Q^*. However, the conceptual model for ET suggests a cause-consequence relation between ET and *VPD*. This is incorrect, as *VPD* itself also is a consequence of Q^*, and therefore ET and *VPD* are merely correlated, and only to some extent.
- The diurnal maximum of *VPD* has a time delay with respect to the maximum of Q^* - and consequently also with respect to the maximum of L_vE. This time delay - that is set by the varying storage of heat in the evolving BL. The existence of this time delay inherently sets the first order effect of ET-*VPD* hysteresis, where the extent of the time delay sets the hysteresis magnitude, as also demonstrated by Zhang et al. (2014).

Therefore the conceptual model neglects the first order effect for the onset and magnitude of ET-*VPD* hysteresis, and its interpretive power is limited. Having said that, under similar climatic and surface circumstances, the ET-*VPD* time lag will remain approximately the same. Hence the model can still be used to demonstrate how a diurnal evolution of r_s - and to a lesser extent r_a - adds to the basic hysteresis effect. Hence it can be concluded that ET-*VPD* hysteresis is a compound effect of the Q^*-*VPD* time lag *and* of the relative diurnal courses of r_s and r_a.

Secondly, to demonstrate variations in hysteresis shape, r_a and r_s are assumed constant throughout the day; where the magnitude of r_s only increases in the afternoon due to stress in terms of temperature, *VPD*, or soil moisture availability. However, under the conditions of the reference case Figure 3.7 shows a clear diurnal course for both resistances: r_a is driven by variations in wind and atmospheric stability, while the behaviour for r_s is dominated by the diurnal cycle of *PAR*. This finding opposes the constant value assumption. Nevertheless, however simplified the behaviour of the variables in the model is, the impact of strong variations in the resistances and *VPD* can still be evaluated conceptually, as in shown in the discussions in Chapters 1.2.2, 3.3.1, 3.3.4, and 3.3.5.

Bibliography

[1] E. Barbaro, J. Vilà-Guerau de Arellano, H. G. Ouwersloot, J. S. Schröter, D. P. Donovan, and M. C. Krol. Aerosols in the convective boundary layer: Shortwave radiation effects on the coupled land-atmosphere system. *J. Geophys. Res. Atmos.*, 119:5845–5863, 2014.

[2] M.T. Chahine. The hydrological cycle and its influence on climate. *Nature*, 359(6394): 373—380, 1992.

[3] L. X. Chen, Z. Q. Zhang, Z. D. Li, J. W. Tang, P. Caldwell, and W. J. Zhang. Biophysical control of whole tree transpiration under an urban environment in northern china. *J. Hydrol.*, 402:388–400, 2011.

[4] R.B. Clapp and G.M. Hornberger. Empirical equations for some soil hydraulic properties. *Water Resour. Res.*, 14:601–604, 1978.

[5] Climate-data.org. Climate selhausen, 2019. URL `https://en.climate-data.org/europe/germany/north-rhine-westphalia/selhausen-117689/`. Last accessed 26 March 2019.

[6] M. Combe, J. Vilà-Guerau de Arellano, H.G. Ouwersloot, and W. Peters. Plant water-stress parameterization determines the strength of land–atmosphere coupling. *Agric. For. Meteorol.*, 217:61–73, 2016.

[7] I. R. Cowan and G. D. Farquhar. *Stomatal function in relation to leaf metabolism and environment, in integration of activity in the higher plant.* Cambridge Univ. Press, edited by D. H. Jehnnings, pp. 471–505, Cambridge, 1977.

[8] D. Doley. Water relations of eucalyptus marginata sm. under natural conditions. *Br. Ecol. Soc. Symp.*, 55:597–614, 1967.

[9] B. E. Ewers, S. T. Gower, B. Bond-Lamberty, and C. K. Wang. Effects of stand age and tree species on canopy transpiration and average stomatal conductance of boreal forests. *Plant Cell Environ.*, 28:660–678, 2005.

[10] J.R. Garratt and B.B. Hicks. Momentum, heat and water vapour transfer to and from natural and artificial surfaces. *Q. J. Roy. Meteor. Soc.*, 99:680–687, 1973.

[11] B. Ghildyal and R. Tripathi. *Soil Physics*. Wiley, New York, 1987.

[12] J. Goudriaan. A simple and fast numerical method for the computation of daily totals of crop photosynthesis. *Agric. For. Meteorol.*, 38:249–254, 1986.

[13] A. Graf, A. Van de Boer, A. Moene, and H. Vereecken. Intercomparison of methods for the simultaneous estimation of zero-plane displacement and aerodynamic roughness length from single-level eddy-covariance data. *B.L.M.*, 151:387, 2014.

[14] M.V. Gutiérrez, F.C. Meinzer, and D.A. Grantz. Regulation of transpiration in coffee hedgerows: covariation of environmental variables and apparent responses of stomata to wind and humidity. *Plant Cell Environ.*, 17:1305–1313, 1994.

[15] I. M. Held and B. J. Soden. Water vapor feedback and global warming. *Annu. Rev. Energy Environ.*, 25(1):441–475, 2000.

[16] T.C. Hsiao. Plant responses to water stress. *Annu. Rev. Plant Physiol.*, 2524:519–570, 1973.

[17] C.M.J. Jacobs. *Direct impact of atmospheric C02 enrichment on regional transpiration*. PhD thesis, Wageningen University, 1994.

[18] C.M.J. Jacobs and H.A.R. De Bruin. Predicting regional transpiration at elevated atmospheric co2: influence of the pbl-vegetation interaction. *J. Appl. Meteorol.*, 36:1663–1675, 1997.

[19] P. G. Jarvis and K. G. McNaughton. Stomatal control of transpiration: Scaling up from leaf to region. *Adv. Ecol. Res.*, pages 1–49, 1986.

[20] G. G. Katul, R. Oren, S. Manzoni, C. Higgins, and M. B. Parlange. Evapotranspiration: A process driving mass transport and energy exchange in the soil-plant-atmosphere-climate system. *Rev. Geophys.*, 50:RG3002, 2012.

[21] R. Leuning. A critical appraisal of a combined stomatal photosynthesis model for c3 plants. *Plant Cell Environ.*, 18:339–355, 1995.

[22] D.K. Lilly. Models of cloud-topped mixed layers under strong inversion. *Quart. J. Roy. Meteor.Soc.*, 94:292–309, 1968.

[23] L. Mahrt. Surface heterogeneity and the vertical structure of the boundary layer. *B.L.M.*, 96:33–62, 2000.

[24] E. Malek. Comparison of the bowen ratio–energy balance and stability-corrected aerodynamic methods for measurement of evapotranspiration. *Theor. Appl. Climatol.*, 48(2-3): 167–178, 1993.

[25] J. Marhsall and R. A. Plumb. *Atmosphere, ocean and climate dynamics: an introductory text*. Elsevier Academic Press, London, 1989.

[26] F. C. Meinzer, G. Goldstein, A. C. Franco, M. Bustamante, E. Igler, P. Jackson, L. Caldas, and P. W. Rundel. Atmospheric and hydraulic limitations on transpiration in brazilian cerrado woody species. *Funct. Ecol.*, 13:273–282, 1999.

[27] F.C. Meinzer, G. Goldstein, P. Jackson, N.M. Holbrook, M.V. Gutiérrez, and J. Cavelier. Environmental and physiological regulation of transpiration in tropical forest gap species: the influence of boundary layer and hydraulic properties. *Oecologia*, 101:541–522, 1995.

[28] G. Miranda García. Cloudroots: an integrated measurement and 0-d modelling approach of vegetation-atmosphere interactions, 2019. MSc Thesis, Wageningen University.

[29] A. F. Moene and J. C. Van Dam. *Transport in the atmosphere-vegetation-soil continuum*. Cambridge University Press, New York, 2014.

[30] C. H. Moeng and J.C. Wyngaard. Statistics of conserved scalars in the convective boundary layer. *J. Atmos. Sci.*, 41:3161–3169, 1984.

[31] P. Ney and A. Graf. High-resolution vertical profile measurements for carbon dioxide and water vapour concentrations within and above crop canopies. *B.L.M.*, 166:449–473, 2018.

[32] J. J. O'Brien, S. F. Oberbauer, and D. B. Clark. Whole tree xylem sap flow responses to multiple environmental variables in a wet tropical forest. *Plant Cell Environ.*, 27: 551–567, 2004.

[33] A.P. O'Grady, D. Eamus, and L.B. Hutley. Transpiration increases during the dry season: patterns of tree water use in eucalypt open-forests of northern australia. *Tree Physiol.*, 19:591–598, 1999.

[34] A.P. O'Grady, D. Worledge, and M. Battaglia. Constraints on transpiration of eucalyptus globulus in southern tasmania, australia. *Agric. For. Meteorol.*, 148:453—465, 1999.

[35] A. Panwar, A. Kleidon, and M. Renner. Do surface and air temperatures contain similar imprints of evaporative conditions? *Geophys. Res. Let.*, 46(7):3802—3809, 2019.

[36] M. B. Parlange, W. E. Eichinger, and J. D. Albertson. Regional-scale evaporation and the atmospheric boundary layer. *Rev. Geophys.*, 33(1):99—124, 1995.

[37] X. Pedruzo-Bagazgoitia. Diffuse radiation in boundary layer cloud-vegetation feedbacks, 2015. MSc Thesis, Wageningen University.

[38] R. A. Pielke Sr. Influence of the spatial distribution of vegetation and soils on the prediction of cumulus convective rainfall. *Rev. Geophys.*, 39(2):151—177, 2001.

[39] R.J. Ronda, H.A.R. De Bruin, and A.A.M. Holtslag. Representation of the canopy conductance in modeling the surface energy budget for low vegetation. *J. Appl. Meteorol.*, 40:1431—1444, 2001.

[40] T. Schneider, P. A. O'Gorman, and X. J. Levine. Water vapor and the dynamics of climate changes. *Rev. Geophys.*, 48:RG3001, 2010.

[41] P.J. Sellers, R. E. Dickinson, D. A. Randall, A. K. Betts, F. G. Hall, J. A. Berry, G. J. Collatz, A. S. Denning, H. A. Mooney, C. A. Nobre, N. Sato, C. B. Field, and A. Henderson-Sellers. Modeling the exchanges of energy, water, and carbon between continents and the atmosphere. *Science*, 275(5299):502—509, 1997.

[42] S. C. Sherwood, R. Roca, T. M. Weckwerth, and N. G. Andronova. Tropospheric water vapor, convection, and climate. *Rev. Geophys.*, 48:RG2001, 2010.

[43] P. C. Stoy, M. Mauder, T. Foken, B. Marcolla, E. Boegh, A. Ibrom ..., and A. Varlagin. A data-driven analysis of energy balance closure across fluxnet research sites: The role of landscape scale heterogeneity. *Agr. For. Meteor.*, 171-172:137–152, 2013.

[44] R.B. Stull. *An introduction to boundary-layer meteorology*. Kluwer Academic, Dordrecht, 1988.

[45] K. Takagi, T. Tsuboya, and H. Takahashi. Diurnal hystereses of stomatal and bulk surface conductances in relation to vapor pressure deficit in a cool-temperate wetland. *Agric. For. Meteorol.*, 91(3-4):177–191, 1998.

[46] H. Tennekes. A model for the dynamics of the inersion above a convective boundary layer. *J. Atmos. Sci.*, 30:558–567, 1973.

[47] A. Tuzet, A. Perrier, and R. Leuning. A coupled model of stomatal conductance, photosynthesis and transpiration. *Plant Cell Environ.*, 26:1097–1116, 2003.

[48] M. H. Unsworth, N. Phillips, T. Link, B. J. Bond, M. Falk, M. E. Harmon, T. M. Hinckley, D Marks, and K. T. Paw Ui. Components and controls of water flux in an old-growth douglas-fir-western hemlock ecosystem. *Ecosystems*, 7:468–481, 2004.

[49] C.C. Van Heerwaarden. *Surface evaporation and water vapor transport in the convective boundary layer*. PhD thesis, Wageningen University, 2011.

[50] C.C. Van Heerwaaren, J. Vilà-Guerau de Arellano, F.G. Amanda Gounou, and F. Couvreux. Understanding the daily cycle of evapotranspiration: A method to quantify the influence of forcings and feedbacks. *Plant Cell Environ.*, 11(6):1405–1422, 2010.

[51] J. Vilà-Guerau de Arellano, C.C. Van Heerwaarden, B.J.H. Van Stratum, and K. Van den Dries. *Atmospheric Boundary Layer: Integrating air chemistry and land interactions*. Cambridge University Press, New York, 2015.

[52] C. Von Hebel, M. Matveeva, E. Verweij, P. Rademske, M. S. Kaufmann, C. Brogi ..., and J. Van der Kruk. Understanding soil and plant interaction by combining ground-based quantitative electromagnetic induction and airborne hyperspectral data. *Geophys. Res. Let.*, 45(15):7571–7579, 2018.

[53] K. C. Wang and R. E. Dickinson. A review of global terrestrial evapotranspiration: Observation, modeling, climatology, and climatic variability. *Rev. Geophys.*, 50:RG2005, 2012.

[54] S. D. Wullschleger, P. J. Hanson, and T. J. Tschaplinski. Whole-plant water flux in understory red maple exposed to altered precipitation regimes. *Tree Phys.*, 18:71–79, 1998.

[55] M. J. B. Zeppel, B. R. Murray, C. Barton, and D. Eamus. Seasonal responses of xylem sap velocity to vpd and solar radiation during drought in a stand of native trees in temperate australia. *Funct. Plant Biol.*, 531:461–470, 2004.

[56] Q. Zhang, S. Manzoni, G. Katul, A. Porporato, and D. Yang. The hysteretic evapotranspiration—vapor pressure deficit relation. *J. Geophys. Res. Biogeosci.*, 119: 125–140, 2014.

[57] H. Zheng, Q. Wang, X. Zhu, Y. Li, and G. Yu. Hysteresis responses of evapotranspiration to meteorological factors at a diel timescale: Patterns and causes. *PLoS ONE*, 9(6): e98857, 2014.